Direct numerical simulation of a non-isothermal non-adiabatic packed bed reactor

Chemical Engineering Journal 385 (2020) 123641

Contents lists available at ScienceDirect

Chemical Engineering Journal

journal homepage: www.elsevier.com/locate/cej

Direct numerical simulation of a non-isothermal non-adiabatic packed bed reactor

V. Chandra, E.A.J.F. Peters*, J.A.M. Kuipers

Multiphase Reactors Group, Department of Chemical Engineering & Chemistry, Eindhoven University of Technology, P.O. Box 513, 5600 MB Eindhoven, The Netherlands

HIGHLIGHTS

- A novel numerical technique to simulate exothermic catalytic packed bed reactors.
- Fluid phase and solid phase events are intrinsically coupled.
- Ignition/Extinction phenomena due to the multiplicity of steady states are captured.
- The hot-spot formation in a wall cooled reactor is analyzed.
- The model is free of empiricism with results dependent only on transport and kinetic values.

ARTICLE INFO

Keywords:
Direct numerical simulation
Packed bed reactors
Immersed Boundary Method
Hot-spot
Heat and mass transfer

ABSTRACT

A fundamental continuum-based numerical model was developed to simulate a non-isothermal non-adiabatic reactor which does not employ any empirical closures. The model was able to capture unique features of an exothermic catalytic reactor such as parametric sensitivity, hot-spot formations and multiplicity of steady states. Furthermore, the model inherently accounts for the various aspects of classical phenomenological models such as axial and radial dispersion of heat and mass and the intrinsic coupling of heat and mass transport between the fluid phase and the solid phase. The numerical procedure was validated with existing literature data before moving on to the simulation of a bed consisting of 340 spherical particles packed using the Discrete Element Method. Five simulations were performed by varying the rate of reaction and keeping all other parameters constant to capture the ignition/extinction phenomena exhibited by exothermic packed bed reactors.

1. Introduction

Tubular packed bed reactors have been widely used in the chemical process industry for decades in various chemical conversion processes such as the selective oxidation of ethylene [1], oxidative coupling of methane [2] and the synthesis of phthalic anhydride [3]. Multi-tubular packed-bed reactors are generally preferred for exothermic reactions where a cooling jacket enclosing the tubular wall is used for controlling the reactor temperature. Highly exothermic systems employ a multi-tubular design where each individual tube has a low tube-to-particle diameter ratio to ensure sufficient cooling across the entire length of the reactor. The dynamics of the non-isothermal reactor are described by non-linear partial differential equations having an Arrhenius type dependency for the rate of reaction and the heat production terms. The intrinsic two-way coupling between temperature and concentration along with the self-dependency of temperature on the heat produced during exothermic reactions causes the system to exhibit many unique features, such as a small change in the inlet feed concentration or temperature that can cause a dramatic change in the reactor effluent conditions, a phenomenon termed *parametric sensitivity* by Bilous and Amundson [4] who were the first to characterize it. If the system exhibits a large transient temperature rise it is generally said to be in a state of *ignition* and analogously if the system cools rapidly, the system is in a state of *extinction*. In the non-adiabatic case, if the reactor does get ignited, the fluid phase temperature profile exhibits a maximum along the axial direction, generally termed *hot-spot* formation in a packed bed reactor. Also, if there exists a sufficient amount of thermal feed-back the reactor may exhibit multiple steady states depending on how the reactor was started up [5]. The non-linearity of the differential equations describing non-isothermal catalytic processes has proven to make it extremely challenging to analyze them analytically, if not impossible. Thus the numerical treatment of these differential equations

* Corresponding author.
E-mail address: e.a.j.f.peters@tue.nl (E.A.J.F. Peters).

https://doi.org/10.1016/j.cej.2019.123641
Received 20 August 2019; Received in revised form 6 November 2019; Accepted 28 November 2019
Available online 02 December 2019

Nomenclature

$\bar{v}$	velocity, m/s
ρ_f	fluid phase density, $\frac{kg}{m^3}$
μ	fluid phase dynamic viscosity, $\frac{kg}{ms}$
C_{pf}	fluid phase specific heat capacity, $\frac{J}{kg\,K}$
k_f	fluid phase thermal conductivity, $\frac{W}{mK}$
D_f	fluid phase molecular diffusivity, $\frac{m^2}{s}$
c_f	fluid phase concentration, $\frac{mol}{m^3}$
T_f	fluid phase temperature, K
ρ_s	solid phase density, $\frac{kg}{m^3}$
C_{ps}	solid phase specific heat capacity, $\frac{J}{kg\,K}$
k_s	solid phase thermal conductivity, $\frac{W}{mK}$
D_s	solid phase molecular diffusivity, $\frac{m^2}{}$s
c_s	solid phase concentration, $\frac{mol}{m^3}$
T_s	solid phase temperature, K
r_s	volumetric rate of reaction inside the solid phase, $\frac{mol}{m^3\,s}$
k	first order reaction rate constant, 1/s
A	Arrhenius pre-exponential factor, 1/s
E	activation energy, J/mol
R	universal gas constant, $\frac{J}{mol\,K}$
r	radial coordinate, m
R_{sp}	radius of sphere, m
c_o	reference/inlet concentration, $\frac{mol}{m^3}$
T_o	reference/inlet temperature, K
ΔH	heat of reaction, J/mol
c_{avg}	averaged surface concentration across the solid phase, $\frac{mol}{m^3}$
T_{avg}	averaged surface temperature across the solid phase, K
k_m	mass transfer coefficient, m/s
h_f	heat transfer coefficient, $\frac{W}{m^2\,K}$
T_{max}	maximum temperature within the system, K
T_b	velocity averaged bulk temperature, K
c_b	velocity averaged bulk concentration, $\frac{mol}{m^3}$
$\langle c_f \rangle$	bulk fluid film concentration, $\frac{mol}{m^3}$
$\langle T_f \rangle$	bulk fluid film temperature, K
V_s	volume of solid phase, m^3
A_s	surface area of solid phase, m^2
A_{cyl}	inner surface area of tubular column, m^2
v_{in}	inlet velocity, m/s
S_f	cross-sectional surface area occupied by the fluid along the column, m^2
R_{cyl}	radius of cylindrical column, m
d_{sp}	diameter of sphere, m
T_{cyl}	cylindrical wall temperature, K
h_w	wall-to-bed heat transfer coefficient, $\frac{W}{m^2\,K}$
j	mass flux, $\frac{mol}{m^2\,s}$
G	number of grid cells across the radius, –
N	number of particles across the tubular column, –
p	pressure, $\frac{kg}{m\,s^2}$
η	particle effectiveness factor, –
ϕ	Thiele modulus, –
k_o	reaction rate constant at reference temperature, 1/s
ϕ_o	Thiele modulus at reference temperature, –
$\bar{\eta}$	reactor bed effectiveness factor, –
k_r	effective radial thermal conductivity, $\frac{W}{mK}$
Re	Reynolds number, –
Nu	fluid-to-particle heat transfer Nusselt number, –
Nu_w	wall-to-bed heat transfer Nusselt number, –
Sh	Sherwood number, –
Bi_h	heat transfer Biot number, –
Bi_m	mass transfer Biot number, –
ν	fluid phase kinematic viscosity, $\frac{m^2}{s}$
L	reactor bed length, m
D_{ax}	axial mass dispersion coefficient, $\frac{m^2}{s}$
k_{ax}	axial thermal dispersion coefficient, $\frac{W}{mK}$
ε_s	catalyst porosity, –
τ_s	catalyst tortuosity, –
ε	reactor bed void fraction, –
γ	Arrhenius number, –
β	Prater number, –
Pr	Prandtl number, –
Sc	Schmidt number, –
Le	Lewis number, –
$\bar{C}_f$	1-D model fluid phase concentration, $\frac{mol}{m^3}$
$\bar{C}_s$	1-D model particle phase concentration, $\frac{mol}{m^3}$
$\bar{T}_f$	1-D model fluid phase temperature, K
$\bar{T}_s$	1-D model solid phase temperature, K

has attracted the interest of chemical engineers for over half a century due to their complexity and importance in reactor design.

Following the seminal contributions by Bilous and Amundson [4] on reactor stability and Van Heerden [5] on heat balance diagrams, many models were developed over the forthcoming decades to determine the performance of an exothermic catalytic reactor. The starting point was the simple one-dimensional homogeneous model used in the aforementioned works where no discrimination was made between the fluid and solid phases. It was shown by Weisz and Hicks [6] that a single catalyst pellet can exhibit the similar dynamics as a homogeneous reactor if intra-particle gradients are non-negligible and the analogous case for inter-phase gradients was demonstrated by Cresswell [7]. This paved the way for the 1-D heterogeneous reactor model [8–10] where the fluid and catalyst phases were distinguished but coupled via a heat and mass transfer term. Simultaneously, two-dimensional models [11,12] were developed to account for radial gradients of concentration and temperature and wall-to-bed heat transfer . This enhanced the predictive capabilities of the model for a non-isothermal non-adiabatic catalytic reactor [13]. However there still seemed to be inconsistencies in the quantitative results of the 2-D model with its experimental counterpart as noted by Paterson and Carberry [14] and they attributed the unsatisfactory agreements to the empirical transport coefficients used in the contemporary models. Lerou and Froment [15] indicated that the effective radial thermal conductivity k_r and the wall-to-bed heat transfer coefficient h_w, which essentially control the magnitude of the hot-spot, needed revision and suggested that the *plug-flow* assumption widely used in phenomenological models needed to be dispensed with and the radial profile of axial velocity should be considered. This was substantiated by other works that had revealed the radial distribution of porosity [16] in a packed bed and consequently a radially varying effective stagnant thermal conductivity [17]. Kaltho and Vortmeyer [18] performed simulations of the ignition and extinction phenomena in an exothermic fixed bed reactor by considering the radial variations of porosity, effective thermal conductivity and velocity. Vortmeyer and Schuster [19] developed a semi-analytical expression for the radial variation of the axial superficial velocity in a packed bed of spheres so as to account for the velocity 'hump' near the wall, sometimes also referred to as flow by-pass or channeling. It was suggested by Cheng and Vortmeyer [20] that flow maldistribution significantly influences the estimation of the hot-spot magnitude as the magnitude of channeling directly influences tranverse thermal dispersion which provides a supplementary resistance in the heat removal

process near the wall. This led Vortmeyer and Haidegger [21] to propose a model where the wall-to-bed heat transfer coefficient was completely discarded and an accurate incorporation of the radial distribution of velocity, porosity and dispersion coefficients was suggested for the evaluation of the non-isothermal non-adiabatic reactor. A more comprehensive literature survey of the radial heat transfer problem may be found in Dixon [22].

As the level of sophistication involved in the description of fixed bed reactors increased, the number of parameters required to close the complex system of equations increased simultaneously. Winterberg et al. [23] provided a review of empirical coefficients determined under non-reactive conditions required for the design of a reactor randomly packed with spherical particles and concluded that the usage of the examined correlations were sufficient to accurately capture transport phenomena of a reactor undergoing chemical reactions. While these empirical coefficients are still widely used in the design of industrial reactors, the validity of these correlations has been eyed with skepticism [24,22].

Inreased advances in computational resources over the last few decades have enabled the simulation of pore-scale resolved transport of momentum, heat and mass in dense gas-solid systems [25]. Direct numerical simulation (DNS) broadly refers to the numerical study of the fundamental continuum based transport equations where the fluid and solid phase transport are fully resolved. These models account for the local interaction between each particle and the surrounding fluid by directly imposing the appropriate boundary conditions along the fluid-solid interface across the entire computational domain, whereas the traditional reaction engineering models account for these interactions in a homogenized manner using empirical correlations. The smoothing out of these local heterogeneities can have a significant influence on the macroscopic performance of the system [26] and the effect of homogenization can be evaluated by performing DNS of the fluid-solid system and use concepts of volume-averaging theory to determine the corresponding empirical values; ex: drag correlation [27], heat and mass transfer coefficient [28], wall-to-bed heat transfer coefficient [29], dispersion coefficients [30] etc. Though a fully resolved simulation of a large scale fixed bed reactor is still a daunting prospect, the level of intricacy of the DNS model in describing transport phenomena such as multi-component diffusion, compressibility, non-ideality, etc., has a large room for improvement [25].

A review of the state-of-the-art simulations conducted on packed bed reactors was presented by Dixon et al. [31] and more recently by Jurtz et al. [32]. Some of the early DNS studies on packed bed reactors neglected intra-particle transport due to the difficulty in meshing the solid phase regions using commercial codes [33]. Recently, there have been several studies which have successfully simulated the intra-particle reaction-diffusion mechanism [34–36] with Maffei et al. [36] introducing a technique which treat the solid and gas phase events individually and then iteratively solved to enforce continuity of fluxes between the two phases. There have been other studies where detailed kinetics have been coupled with pore-scale simulations for endothermic reactions such as dry reforming of methane [33,37]. However, there exist very few studies which directly tackle the exothermic case where coupled intra-particle heat and mass transfer gradients are considered with the recent work by Partopour and Dixon [38] being one. The primary objective of this work is to develop a model devoid of empiricism and yet capture all the essential characteristics manifested by a packed bed reactor undergoing exothermic reactions.

In this manuscript we expand upon the work of Das et al. [29] where flow and heat transfer was studied in a cylindrical column packed with spherical particles using the Discrete Element Method (DEM). Here, we consider intra-particle diffusion of heat and mass along with a simple first-order irreversible reaction governed by the Arrhenius equation. This paper extends on the model developed by Lu et al. [39] where an isothermal surface reaction is considered and Lu et al. [40] where an exothermic non-isothermal surface reaction governed by the Arrhenius equation is considered. Here, a volumetric reaction within the solid phase is considered where a novel fluid-solid coupling technique is presented with the dynamic issues of ignition/extinction which arises from the intrinsic coupling between the gas and solid phase events are addressed. The basis of our DNS technique is the Immersed Boundary Method (IBM), which is used for enforcing the appropriate boundary conditions along the fluid-solid interface and the wall enclosing the bed. In Section 2 we present the governing system of equations and boundary conditions used for simulating the packed bed reactor. Subsequently, the numerical procedure is described followed by an explanation of the Immersed Boundary Method. The numerical procedure is validated in Section 3 and the results of the full bed simulations are discussed in Section 4.

2. Governing equations and numerical details

2.1. Model description

The artificially generated fixed bed consists of 340 spheres randomly packed in a slender tubular column using the DEM approach. The tube-to-particle diameter ratio is 5 and the details of the packing procedure may be found in Das et al. [29]. The DEM packing is mapped on to the computational domain where the following system of equations are solved on a uniform 3-dimensional Cartesian grid. The mass and momentum balance for an incompressible Newtonian fluid reads

$$\nabla\cdot\bar{v} = 0 \tag{1}$$

$$\rho_f \frac{\partial \bar{v}}{\partial t} + \rho_f \nabla\cdot(\bar{v}\bar{v}) = -\nabla p - \nabla\cdot\bar{\bar{\tau}} \tag{2}$$

where ρ_f and μ represent the fluid's density and viscosity rescpectively and $\bar{\bar{\tau}}$ is the stress tensor with $\bar{\bar{\tau}} = -\mu[\nabla\bar{v} + (\nabla\bar{v})^T]$.

The no-slip boundary condition is enforced along the solid interface of the spherical catalyst particles and the cylindrical wall with

$$\bar{v} = 0 \text{on} A_s \quad \text{and} \quad A_{cyl} \tag{3}$$

where A_s refers to the surface area of the solid particles within the tubular column and A_{cyl} refers to the inner surface area of the cylidrical wall enclosing the catalyst particles.

The fluid phase governing equations for concentration and temperature are

$$\frac{\partial c_f}{\partial t} + \nabla\cdot\bar{v}c_f = \nabla\cdot D_f \nabla c_f \tag{4}$$

$$\rho_f C_{pf} \frac{\partial T_f}{\partial t} + \nabla\cdot\bar{v}T_f = \nabla\cdot\ k_f \nabla T_f \tag{5}$$

Here D_f is the molecular diffusivity of the reactant in the fluid phase and k_f and C_{pf} are the thermal conductivity and the specific heat capacity of the fluid respectively. The solid phase governing equations are

$$\frac{\partial c_s}{\partial t} = \nabla\cdot D_s \nabla c_s + r_s \tag{6}$$

$$\rho_s C_{ps} \frac{\partial T_s}{\partial t} = \nabla\cdot\ k_s \nabla T_s + (\Delta H) r_s \tag{7}$$

Here D_s is the effective molecular diffusivity of the reactant in the solid phase where $D_s = \frac{\varepsilon_s}{\tau_s} D_f$ with ε_s and τ_s referring to the internal porosity and tortuosity of the catalyst particles. Usually, the values of ε_s and τ_s are determined experimentally, but in all the numerical studies performed here we consider the value of $\frac{\varepsilon_s}{\tau_s} = \frac{D_s}{D_f}$ to be some predetermined value. k_s, ρ_s and C_{ps} refer to the thermal conductivity, density and the specific heat capacity of the solid phase respectively. r_s is the rate of reaction and ΔH is the heat of reaction whose value is negative for exothermic reactions.

We restrict our analyses to an irreversible first-order reaction given as

$$r_s = -kc_s \tag{8}$$

where k is the first-order rate constant of the reaction and the negative sign in the above equation refers to the consumption of the reactant within the solid phase. We further consider the non-linear coupling between the rate constant and the local temperature in the catalyst phase given by the Arrhenius equation

$$k = Ae^{\frac{-E}{RT_s}} \tag{9}$$

Here, E refers to the activation energy of the reaction with R being the universal gas constant and A is the Arrhenius pre-exponential factor.

Furthermore, we assume there is continuity of fluxes between the fluid phase and the solid phase and thus we impose the interface boundary condition for the scalar transport variables as follows

$$-D_f \nabla c_f \cdot \bar{n} = -D_s \nabla c_s \cdot \bar{n}; \quad c_f = c_s \text{ on } A_s \tag{10}$$

$$-k_f \nabla T_f \cdot \bar{n} = -k_s \nabla T_s \cdot \bar{n}; \quad T_f = T_s \text{ on } A_s \tag{11}$$

Finally, we model the tube wall to provide a cooling effect across the entire packed bed. Thus we impose a constant temperature across the inner face of the cylindrical wall and the wall is assumed to be inert to the reacting species. While the solid particles form one continuous phase, it is assumed that the particles do not touch the inner face of the wall. Thus the cooling of the particles is done via a thin layer of fluid surrounding the wall. The boundary conditions for temperature and species concentration are

$$T_f = T_{cyl} \text{ on } A_{cyl} \tag{12}$$

$$-D_f \nabla c_f \cdot \bar{n} = 0 \text{ on } A_{cyl} \tag{13}$$

Thus having defined the wall boundary conditions, we now have a complete system of equations which may be solved numerically.

2.2. Numerical procedure

The governing equations are solved on a 3-D Cartesian domain employing uniform grids. The initial task is to map the solid phase on to the computational domain which is done by identifying the position of the sphere(s) and then flagging the grid cells with cell centres that lie inside the solid and fluid phases respectively using the analytical expression governing a sphere. The equations governing both the fluid and solid phase are then discretized, followed by the imposition of the wall and interface boundary conditions and then solved simultaneously on a single computational domain. The solution of the momentum, heat and mass transport equations are treated in a sequential manner; i.e., within a single time-step the Navier-Stokes equations are first solved followed by the solution of the fluid and solid phase temperature equations and finally the mass transport equations. While the 3 transport mechanisms (momentum, heat, mass) are decoupled, the fluid phase events and the solid phase events of each transport are coupled and treated in a semi-implicit manner (described below), thus maintaining the stability of the numerical technique. The detailed description of the numerical procedure to solve the Navier-Stokes equations can be found in the works of Deen et al. [41] and Das et al. [29].

The scalar transport equations are solved using a finite volume approach. The discretization schemes used are presented Table (1) where the fluid phase concentration balance equation has been used as an example. In the solids phase, a diffusion-reaction equation is solved for concentration, with both the diffusion and reaction terms evaluated fully implicitly. For all cases considered in this manuscript, the reaction term is linearly dependent on concentration and thus no linearization is required. In the general case of non-linear dependencies of the reaction term on concentration, the iterative Newton-Raphson technique is used. The coupling between the fluid and solid phases is discussed extensively later. Following the solution of the concentration field, the temperature field is then updated. In the fluid phase it obeys a convection-conduction equation that is discretized in the same way as the equation for concentration. The solids phase temperature is governed by a conduction equation that includes a source term. The conduction term is evaluated implicitly and the source term is treated fully explicitly, i.e., the reaction term already computed for the diffusion-reaction equation is just multiplied by the heat of reaction. The heat generated is self-dependent on the temperature value via the Arrhenius relation and the explicit treatment keeps the numerical technique unconditionally stable. A by-product of this unique self-generation source term is the possibility of multiple steady states and is discussed in more detail later. The rate of reaction term is of larger significance as its explicit treatment can cause the numerical technique to become unstable and produce negative values of concentration when the rate of consumption of reactant increases rapidly due to temperature excursions. For first order irreversible reactions, the implicit treatment of the term is again straightforward as $f(c_s)^{n+1} = r_s^{n+1} = -k^{n+1}c_s^{n+1}$ as it is a linear term with k^{n+1} referring to the rate constant evaluated using the recently updated temperature field. All simulations conducted in this manuscript employ an irreversible first order reaction, however, the extension of the methodology to solve complex kinetics with different orders is also presented. In the scenario that the rate of reaction term is non-linear with concentration, a linearization technique would need to be used. This would then require the term, $f(c_s)^{n+1}$, to be first linearized and then solved in iterative manner. This may be done using the classical Newton-Raphson iterative technique.

The discretized form of the p.d.e.'s governing the concentration (fluid and solid) values at all grid nodes across the computational domain of the form shall yield a set of linear algebraic equations

$$a_P c_P + \sum_{nb} a_{nb} c_{nb} = b_P \tag{14}$$

where a_P is the coefficient of the central grid node concentration and b_P is the production term, where both contain linearized parts of the reaction term. '*nb*' refers to the 6 neighboring nodes of the central grid node within the 3-D Cartesian grid and a_{nb} their respective coefficients. The set of linear algebraic equations represented by Eq. (14) is then solved for all grid nodes. It must be noted that the coefficients and the production vector b_P in Eq. (14) have been modified to account for the fluid-solid interactions applied using the Immersed Boundary Method described below. The interaction between the two phases is accounted for such that the coefficient values in Eq. (14) are modified so that the fluid-solid interface transport value is satisfied by changing the transport values in the neighbouring cells.

A crucial component of the numerical procedure is the Immersed Boundary Method [41,42] that is used to enforce the appropriate fluid-solid interface boundary conditions given by Eqs. (10) and (11) and the wall boundary conditions given by Eqs. (12) and (13). The imposition of the no-slip boundary condition for velocity has been described by Das et al. [29] and shall be omitted here. Different types of boundary conditions may be enforced such as the Dirichlet b.c. where a specific constant value is imposed over the entire interface, or the Neumann b.c. (constant flux) or boundary condition of the 4th type (continuity of fluxes). The Dirichlet b.c. forms the base recipe over which the other boundary conditions may be imposed in an extended manner.

For enforcing the Dirichlet b.c., the value of c at the fluid-solid interface is known *a priori*. In Fig. 1a, the solid phase grid node P

Table 1
Discretization schemes used for solving the scalar transport equations.

Term	Discretization	Scheme
$\frac{\partial c}{\partial t}$	$\frac{C_P - C_P^0}{\Delta t}$	Euler forward
$\frac{\partial vc}{\partial x}$	$\frac{v_e c_e - v_W c_W}{\Delta x}$	TVD Min-Mod scheme
$\left(\frac{\partial}{\partial x}\left(D_f \frac{\partial c}{\partial x}\right)\right)$	$D_{f,e}\left(\frac{c_E - e_P}{\Delta x}\right) - D_{f,w}\left(\frac{c_P - c_W}{\Delta x}\right)$	Central differencing scheme

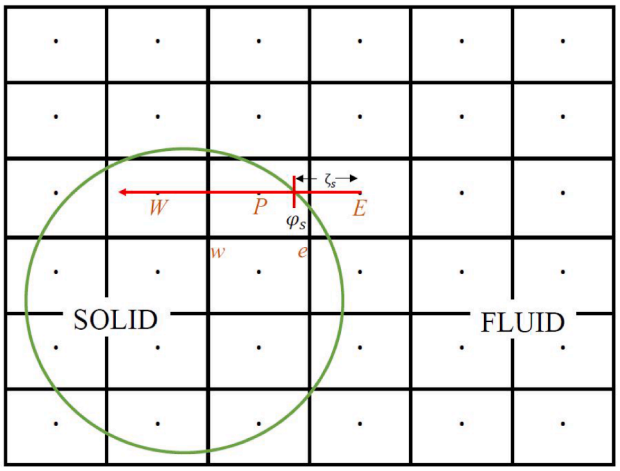

(a) Implementation of the Dirichlet b.c.

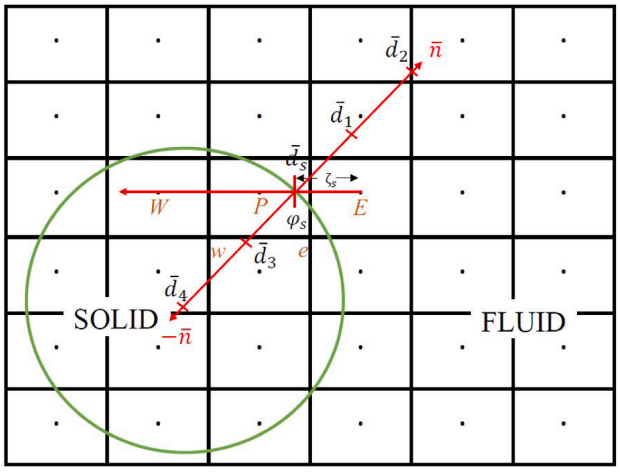

(b) Extension of the Dirichlet b.c.

Fig. 1. Pictorial depiction of the implementation of the Immersed Boundary Method to impose the different fluid-solid interface boundary conditions.

neighbors a fluid node E and another fellow solid node W. The value of c at the solid surface is a known value, indicated by c_S. To enforce the fluid-solid coupling, a directional quadratic fit is used whose procedure may be found in Deen and Kuipers [43]. The directional quadratic fit gives us an expression for concentration c in the fluid node E as follows:

$$c_E = \frac{-2\xi_s}{1-\xi_s}c_P + \frac{\xi_s}{2-\xi_s}c_W + \frac{2}{(1-\xi_s)(2-\xi_s)}c_S \tag{15}$$

The above fit is now used to rewrite the discretized Eq. (14) governing the concentration c in grid node P. This results in a set of modified coefficients for Eq. (14) which reads

$$a_P^{`} = a_P + a_E\left(\frac{-2\xi_s}{1-\xi_s}\right) \tag{16}$$

$$a_W^{`} = a_W + a_E\left(\frac{\xi_s}{2-\xi_s}\right) \tag{17}$$

$$a_E^{`} = 0 \tag{18}$$

$$b_P^{`} = b_P - a_E\left(\frac{2c_S}{(1-\xi_s)(2-\xi_s)}\right) \tag{19}$$

The above set of modified coefficients have now been changed to account for the interface boundary condition for the grid node P that lies in the immediate vicinity of the fluid-solid interface. The above mentioned procedure must be carried out for all such other grid nodes whose neighboring node lies in the opposite phase and for all co-ordinate directions. The methodology explained above used a solid phase grid node P as an example whose neighbor is a fluid phase cell, and the analogous case of a fluid cell whose neighbor is a solid cell also requires the same treatment with a directional fit now pointing in the fluid phase direction.

Other forms of boundary conditions may be represented as follows respectively

$$-D\frac{\partial c}{\partial \bar{n}} = j \text{on} A_s \tag{20}$$

$$-D_f\frac{\partial c}{\partial \bar{n}} = -D_s\frac{\partial c}{\partial \bar{n}};\quad c_f = c_s \text{ on } A_s \tag{21}$$

where D refers to the molecular diffusivity of either the fluid or solid phase denoted by the subscripts f and s respectively. In such cases, the interface value represented by c_S is not known *a priori*. In Fig. 1b we again have a grid node P whose neighbours are a fluid cell E and a solid cell W. The value of the scalar quantity at the fluid-solid intersection point is unknown in this case and must be calculated prior to using the Dirichlet b.c. framework as described earlier. To compute the value at the intersection point indicated by the position vector $\bar{d}_s$, 4 probes normal to the intersection point are drawn such that

$$\bar{d}_1 = \bar{d}_s + (\Delta x)\bar{n},\ \bar{d}_2 = \bar{d}_s + (2\Delta x)\bar{n},\ \bar{d}_3 = \bar{d}_s - (\Delta x)\bar{n},\ \bar{d}_4 = \bar{d}_s - (2\Delta x)\bar{n} \tag{22}$$

Thereby we have 4 probes whose locations are indicated by the position vectors $\bar{d}_1$, $\bar{d}_2$, $\bar{d}_3$ and $\bar{d}_4$ where (Δx) is the Eulerian grid spacing (grid size) to maintain second order accuracy of the numerical procedure as a whole. In order to impose the boundary conditions given by Eqs. (20) and (21), the derivatives are expanded using Taylor series up to the second degree with a step size Δx and may be expressed algebraically as follows

$$-D_f\frac{(4c_1 - c_2 - 3c_S)}{2\Delta x} = j \tag{23}$$

$$-D_f\frac{(4c_1 - c_2 - 3c_S)}{2\Delta x} = -D_s\frac{(4c_3 - c_4 - 3c_S)}{-2\Delta x} \tag{24}$$

where c_1, c_2, c_3 and c_4 refer to the positional values of concentration at the location of $\bar{d}_1$, $\bar{d}_2$, $\bar{d}_3$ and $\bar{d}_4$ respectively. The values of c_1, c_2, c_3 and c_4 are calculated by trilinear interpolation using concentration values at grid positions from the previous time-step. Rearranging Eqs. (23) and (24), we may now estimate the concentration values at the fluid-solid intersection point represented by c_S as follows

$$c_S = \frac{1}{3}\left[4c_1 - c_2 - 2\left(\frac{j}{-D_f}\right)\Delta x\right] \tag{25}$$

$$c_S = \frac{D_f(4c_1 - c_2) + D_s(4c_3 - c_4)}{3(D_f + D_s)} \tag{26}$$

Once the fluid-solid intersection point value is estimated using the above two equations, the aforementioned Dirichlet b.c. framework is applied to impose the appropriate interface boundary conditions.

It must be noted that the above mentioned Immersed Boundary procedure described for concentration may analogously be extended to temperature. During exothermic reactions, there may be large temperature gradients due to the ignition of particles. In such a scenario, there may be sharp spatio-temporal gradients in the solid phase with $T_4 \gg T_3$ which may result in T_S having a negative value. Thus in order to ensure that the fluid-solid interface value does not have a negative value, we may employ a linear interpolation so that the numerical technique reaches the steady state solution in a stable manner. The first order interpolation to estimate the fluid-solid intersection point value is

given by

$$T_S = \frac{k_f T_1 + k_s T_3}{k_f + k_s} \tag{27}$$

It must be noted that the estimation of T_S is treated explicitly, however the fully implicit implementation of the Dirichlet b.c. framework maintains the stability of the procedure. When the particles are fully ignited or extinguished, the spatial gradients inside the catalyst particles are not extremely sharp and the second order interpolation given by Eq. (26) may be used. The switching of the first order estimation to the second order estimation is done when T_S evaluated using Eq. (26) is non-negative with $T_S > 0$. It must also be noted that in many situations the second probe vector normal to the solid surface into the fluid may lie inside another solid particle. In such situations, a first-order interpolation must again be used. The validity of the numerical technique is presented in the next section for various cases.

3. Verification and validation

The validation of the numerical procedure to study non-isothermal reactive transport in a full packed bed reactor is done by validating each key ingredient comprising transport in a packed bed. First, we verify the numerical methodology to study intra-particle mass and heat transport by comparing our results using the Immersed Boundary Method with the classical solutions of Thiele [44] and Weisz and Hicks [6] for a single catalyst pellet. Next, we validate the enforcing of the continuity of fluxes boundary condition via the IBM for cases when there is forced convection around a single spherical catalyst. Subsequently, the enforcing of the cylindrical wall boundary conditions are verified. The validation of the implementation of the Navier-Stokes equations and the fluid phase heat and mass transport equations are not presented in this paper as they have been thoroughly validated previously, and may be found in Das et al. [41,43,42,29].

3.1. Intra-particle heat and mass transport

As an elementary verification case we first numerically simulate intra-particle diffusion and reaction under isothermal conditions. The equation governing the transport in a spherical catalyst is given by

$$\frac{\partial c_s}{\partial t} = \nabla \cdot D_s \nabla c_s - k c_s \tag{28}$$

where k is the isothermal rate-constant, with the boundary condition along the interface of the catalyst

$$c_s = c_o \text{on} A_s \tag{29}$$

The Dirichlet boundary condition assumes that there is no external mass transfer resistance and a constant uniform concentration is present along the interface of the catalyst and radial symmetry is implicitly assumed. The above system is replicated in 3 dimensions as depicted in Fig. 2a with the interface boundary condition enforced using the IBM described in the previous section. The analytical solution for the concentration profile at steady-state is

$$\frac{c_s}{c_o} = \frac{R_{sp}}{r} \frac{\sinh(r\sqrt{k/D_s})}{\sinh(\phi)} \tag{30}$$

where ϕ is the Thiele Modulus [44] and R_{sp} is the radius of the sphere with $\phi = R_{sp}\sqrt{\frac{k}{D_s}}$. The analytically obtained concentration profile is plotted against the concentration profile obtained along the radius of the sphere simulated using DNS and is presented in Fig. 2b for $\phi = 10$. 2 different grid resolutions were used with $G = 10$, 20 where G refers to the number of Eulerian grid cells across the radius of the spherical catalyst. The effectiveness factor of the catalyst is computed as follows

$$\eta = \frac{\iint \int_{V_s} k c_s dV}{\frac{4}{3}\pi R_{sp}^3 k c_o} \tag{31}$$

The analytically derived expression for the effectiveness factor in a spherical catalyst is given by

$$\eta = \frac{3}{\phi^2}(\phi \coth\phi - 1) \tag{32}$$

The effectiveness factor numerically computed using Eq. (31) was compared with the analytical solution of Eq. (32) for varying Thiele moduli. The Thiele Modulus was varied by changing the rate constant values and keeping the radius and diffusivity values constant. The results are plotted in Fig. 3 where all simulations were performed with a grid resolution of $G = 10$. A grid dependency test for $\phi = 2.0$ is presented in Table (2).

The intra-particle mass transport may be coupled with intra-particle heat transport where we consider an exothermic reaction with heat production dependent on the rate of reaction. Eq. (28) is now coupled with the following temperature balance equation given by

$$\rho_s C_{ps} \frac{\partial T_s}{\partial t} = \nabla \cdot k_s \nabla T_s + (\Delta H) k c_s \tag{33}$$

where k is now a non-isothermal rate constant given by the Arrhenius expression described in Eq. (9). Once again, a Dirichlet b.c. is assumed for temperature along the interface of the catalyst particle to replicate the Weisz and Hicks [6] case:

$$T_s = T_o \text{ on } A_s \tag{34}$$

No analytical solution is available for the case considered here due to the Arrhenius coupling between heat and mass, while the numerical

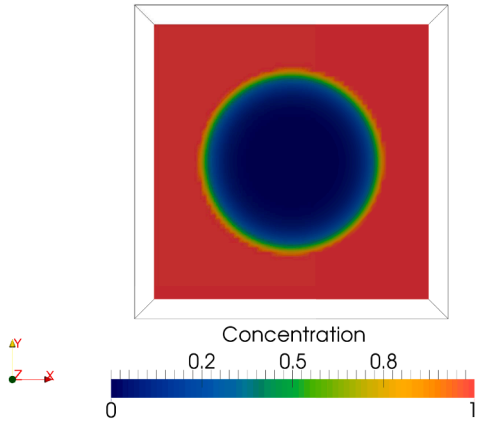

(a) 3-D contour plot simulated using DNS for $\phi = 10.0$.

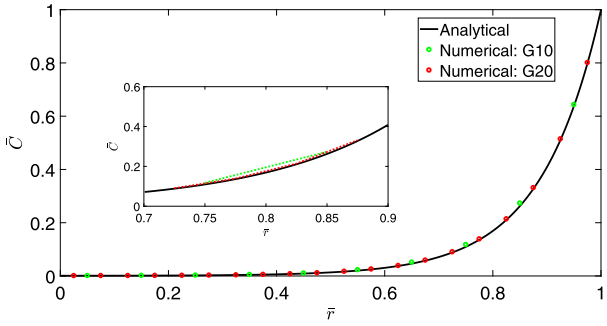

(b) Grid dependency analysis of the concentration profile plotted along the axis of symmetry against the analytical solution.

Fig. 2. Dimensionless concentration profiles for isothermal diffusion and reaction for $\phi = 10.0$.

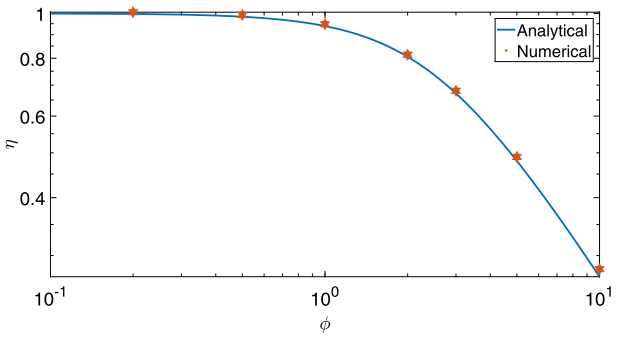

Fig. 3. Validation of the DNS technique for isothermal diffusion and reaction.

Table 2
Grid dependency study for isothermal diffusion and reaction for $\phi = 2.0$.

Grid resolution	η (DNS)	η (Analytical)	Error
$G = 10$	0.8146	0.8060	1.07%
$G = 20$	0.8073	–	0.16%
$G = 40$	0.8060	–	~0%

solutions were originally provided by Weisz and Hicks [6]. The 2 coupled p.d.e.'s under the steady state assumption were transformed into a single o.d.e. as is done in Weisz and Hicks [6] and solved using MATLAB's in-built ode15s solver. The numerically obtained MATLAB results were compared with the numerical results obtained by performing DNS using the Immersed Boundary Method. The rate of heat generation is dependent on temperature as mentioned earlier and intra-particle heat conduction provides a feed-back of heat towards the surface of the particle helping enhance the rate of reaction due to the Arrhenius coupling. This mechanism causes certain cases to have multiple steady states with 2 stable points and one meta-stable point. The meta-stable point is physically unstable and a transient numerical procedure shall not be able to capture these points. The lower steady state is the point of low conversion with very small intra-particle gradients of temperature and concentration, while the higher steady states have effectiveness factors much greater than unity, $\eta \gg 1$, with sharp gradients of temperature and concentration close to the catalyst surface. The multiple steady states are captured by imposing different initial conditions and the convergence to either of the 2 steady states is dependent on the value of the initial particle concentration or temperature. The criteria for multiple steady states were identified by Weisz and Hicks with the help of 2 dimensionless parameters:

$$\gamma = \frac{E}{RT_o} \tag{35}$$

$$\beta = \frac{c_o(-\Delta H)D_s}{k_s T_o} \tag{36}$$

where γ and β are sometimes referred to as the Arrhenius Number and Prater Number respectively. γ is a measure of the rate constant's sensitivity to temperature and β is the dimensionless heat of reaction which is also the maximum dimensionless temperature rise possible within the catalyst pellet ($\beta = \frac{T_{max} - T_o}{T_o}$). The results obtained from DNS are compared with the results of Weisz and Hicks [6] computed using MATLAB in Fig. 4. γ was fixed to be 20, with the value of β varied from $0.4 - 0.8$ for varying Thiele Moduli (ϕ_o). Here the Thiele Modulus is normalized by using the rate constant at surface conditions, k_o, where $\phi_o = R_{sp}\sqrt{\frac{k_o}{D_s}}$ with $k_o = Ae^{\frac{-E}{RT_o}}$. Similarly, the effectiveness factor is calculated as is done for the isothermal case given by Eq. (31), but with $k = k_o$ in this case. The steady state profiles of the multiple solutions of the Weisz and Hicks case captured using DNS are presented in Fig. 5.

3.2. Conjugated mass transport

Intra particle mass transport in packed bed reactors is influenced by the effect of the flow field around the catalysts. Only in rare circumstances can we consider the external mass transfer resistance to be completely neglected such that a uniform concentration around the catalyst is obtained as described by the boundary condition in Eq. (29). That would require the mass transfer Biot Number to be extremely high ($Bi_m \to \infty$). As both internal and external mass transfer limitations exist in common gas-solid heterogeneous catalyzed systems, a more appropriate interface condition is the continuity of fluxes as described in Eq. (10). We may analytically solve Eq. (28) using the following boundary condition:

$$-D_s \nabla c_s \cdot \bar{n} = k_m(c_s - c_o) \text{ on } A_s \tag{37}$$

where k_m is the fluid-to-particle external mass transfer coefficient. Upon non-dimensionalizing, we rewrite the above boundary condition in 1-D spherical coordinates as

$$\frac{\partial \bar{c_s}}{\partial \bar{r}} = Bi_m(1 - \bar{c_s}) \text{ on } A_s \tag{38}$$

where the mass transfer Biot Number (Bi_m) is

$$Bi_m = \frac{k_m R_{sp}}{D_s} \tag{39}$$

The analytically derived expression for the overall effectiveness factor with the above boundary condition is

$$\eta = \frac{3}{\phi^2}\frac{(\phi\coth\phi - 1)}{\left(1 + \frac{(\phi\coth\phi - 1)}{Bi_m}\right)} \tag{40}$$

The enforcing of the continuity of fluxes boundary condition is validated by simulating forced convection around a single stationary sphere with an inlet feed concentration of c_o. Accurate enforcement of the boundary condition given by Eq. (10) will ensure that both the internal and external mass transfer resistances are captured and for a specific value of the Biot Number, the effectiveness factor is calculated and compared with the analytical values given by Eq. (40). The external mass transfer coefficient from the DNS study is calculated by evaluating the mass flux across the surface of the sphere numerically as follows

$$j = \frac{\oint\oint_{A_s} -D_f \nabla c_f \cdot \bar{n} dA}{4\pi R_{sp}^2} \tag{41}$$

with the mass transfer coefficient computed by

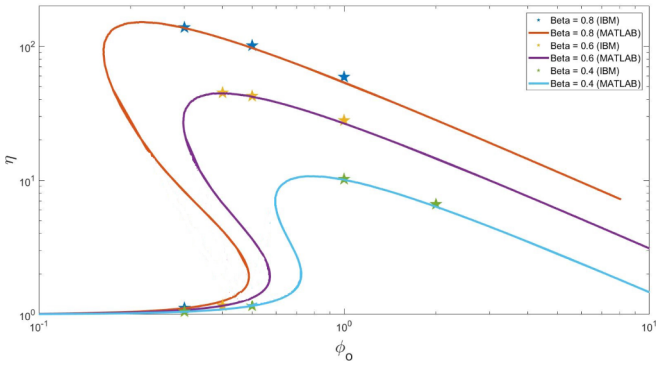

Fig. 4. Validation of the DNS technique with the Weisz and Hicks case for $\gamma = 20$. The $\beta = 0.8$ case and the $\beta = 0.6$ case contain multiple steady states at $\phi_o = 0.3$ and $\phi_o = 0.4$ respectively. $\eta_1 = 1.12$ and $\eta_2 = 138.05$ are the two stable steady state effectiveness factor values for the $\beta = 0.8$, $\phi_o = 0.3$ case with $\eta_3 = 8.16$ being the meta-stable point which cannot be captured using the transient DNS technique. Similarly, $\eta_1 = 1.16$ and $\eta_2 = 44.94$ are the two stable steady states for the $\beta = 0.6$, $\phi_o = 0.4$ case and $\eta_3 = 6.81$ being the meta-stable point.

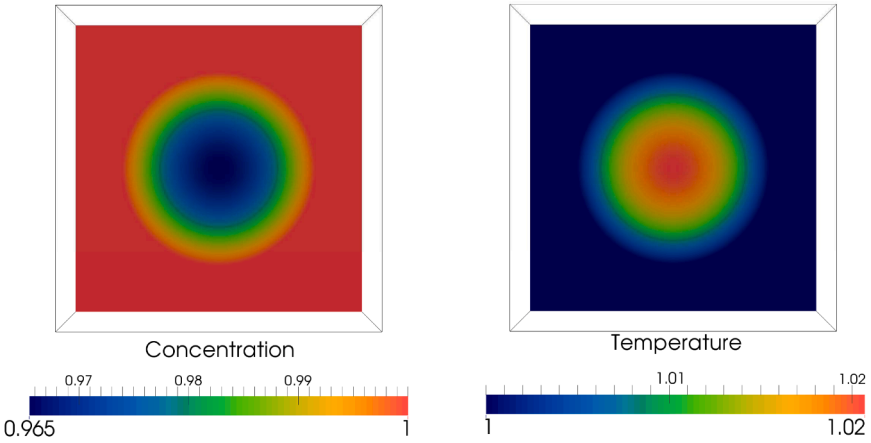

(a) Lower steady state concentration profile with minimal conversion ($\eta = 1.162$).

(b) Lower steady state temperature profile with minimal temperature gradients ($\eta = 1.162$).

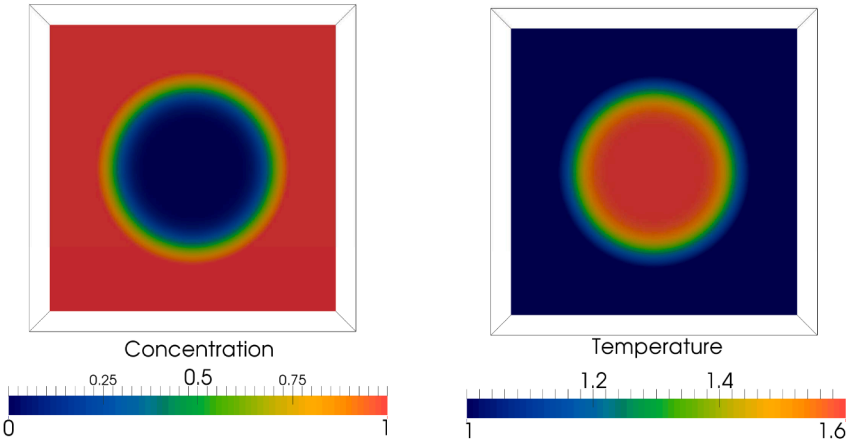

(c) Higher steady state concentration profile with almost complete conversion ($\eta = 44.943$).

(d) Higher steady state temperature profile with a temperature gradient of $\frac{T-T_o}{T_o} = 0.6 = \beta$ with $\eta = 44.943$.

Fig. 5. Dimensionless contour plots of the multiple steady state profiles of the Weisz and Hicks case for $\phi_o = 0.4$, $\gamma = 20$ and $\beta = 0.6$.

$$k_m = \frac{j}{c_o - c_{avg}} \tag{42}$$

where c_{avg} refers to the averaged point concentration values along the interface of the 3 dimensional sphere present within the DNS domain. A similar analysis was performed Sulaiman et al. [45] recently to verify their code.

The fully resolved velocity profile for flow past a single sphere is depicted in Fig. 6a. We may verify the implementation of boundary condition in Eq. (10) by varying the diffusivity in the solid phase, thus changing the Biot Number values to study the effect of internal mass transfer resistances on the effectiveness factor. It must be noted that the rate constant (k) values are changed to ensure that the Thiele Modulus remains constant, with $\phi = 2.0$ for all cases studied. Decreasing the ratio of solid to fluid diffusivities significantly affects the overall effectiveness factor as is evident from Eq. (40), where as $Bi_m \rightarrow \infty$ the effectiveness factor expression results in the more familiar one given in Eq. (32).

In general gas-solid systems, the fluid-solid diffusivities range between 0.1-0.5 and are based on the tortuosity and porosity values of the particle. Here, 3 different ratios of fluid to solid diffusivities (1.0, 0.1, 0.01) were investigated along with the effect of 3 different Reynolds numbers. The computed effectiveness factors and the Sherwood numbers from the DNS study were compared with the analytical solution given by Eq. (40) and the empirical Frossling correlation given by (43) respectively and the results are presented in Table (3). The concentration contour plots are presented in Fig. 6b–d) for the 3 different diffusivity values. It is seen that at $\frac{D_s}{D_f} = 0.01$, an almost uniform concentration profile is formed along the catalyst surface as one would expect. To ensure that the external mass transfer coefficient value calculated is correct, we may compare the values obtained numerically with the empirical Frossling correlation. The Frossling correlation characterizes the external mass transfer resistance for flow past a single sphere with the Sherwood number (Sh) expressed as a function of the Reynolds number (Re):

$$Sh = 2.0 + 0.6Re^{1/2}\,Sc^{1/3} \tag{43}$$

where the Sherwood number is defined as follows

$$Sh = \frac{k_m(2R_{sp})}{D_f} = 2Bi_m\frac{D_s}{D_f} \tag{44}$$

with the Reynolds number given by

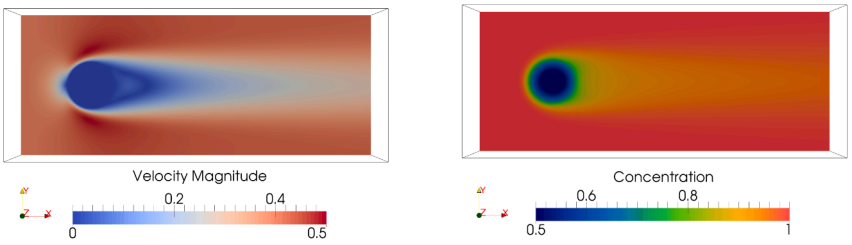

(a) Contour plot of the velocity (m/s) profile for flow past a sphere case.

(b) Dimensionless concentration contours for flow past a sphere for $\frac{D_s}{D_f} = 1.0$.

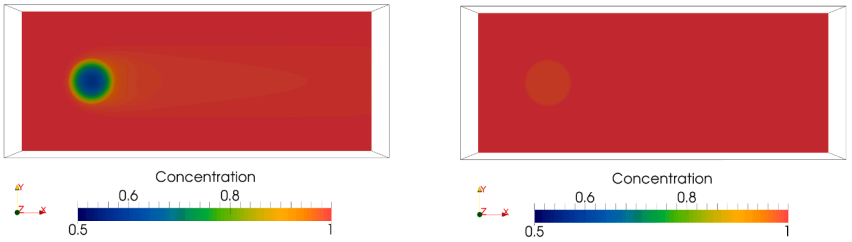

(c) Dimensionless concentration contours for flow past a sphere for $\frac{D_s}{D_f} = 0.1$.

(d) Dimensionless concentration contours for flow past sphere for $\frac{D_s}{D_f} = 0.01$.

Fig. 6. Dimensionless contour plots depicting isothermal reactive transport for a single sphere case, for $Re_p = 80$ and $\phi = 2.0$.

Table 3
Validation of internal and external mass transport for flow past a single sphere for $\phi = 2.0$.

$\frac{D_s}{D_f}$	Re	Bi_m	η(DNS)	η (Analytical)	Sh (DNS)	Sh (Empirical)
1.0	80.0	3.671	0.630	0.624	7.342	7.367
0.1	80.0	36.740	0.785	0.783	7.348	7.367
0.01	80.0	383.45	0.869	0.804	7.669	7.367
0.1	10.0	19.635	0.762	0.764	3.927	3.897
0.1	40.0	29.045	0.780	0.777	5.809	5.795

$$Re = \frac{v_{in}(2R_{sp})}{\nu} \tag{45}$$

In Eq. (43), Sc refers to the Schmidt number which is the ratio of the kinematic viscosity ν to the diffusivity of the fluid (D_f) and $\langle \bar{v} \rangle$ is the inlet velocity. The results of the comparison with the Frossling correlation are also presented in Table (3) and it must be noted that the correlation was experimentally determined for extremely fast surface reactions ($\phi \gg 1$) while we have considered $\phi = 2.0$ for all cases.

3.3. Cylindrical wall boundaries

Cylindrical wall boundaries for the tubular bed are imposed using the Immersed Boundary Method. A Dirichlet boundary condition is used for temperature and a Neumann boundary condition is imposed for concentration. We verified both by simulating a single-phase laminar flow through a cylindrical conduit with the boundary conditions for temperature given by Eq. (12) and by specifying a non-zero finite constant mass flux (j) along A_{cyl}. The Nusselt Number and the Sherwood number can be calculated at the fully developed section of the tube. The Nusselt number for the Dirichlet b.c. case is described by the Graetz-Nusselt problem and the analytically derived value is $Nu = 3.657$. For the constant mass flux case, the Sherwood number is described by the extended Graetz-Nusselt problem [46] and $Sh = 4.364$. The numerically computed values for both the problems is given in Table (4) showing a very good agreement between the simulation results and the 'exact' solutions reported in literature.

4. Results and discussion

Five simulations were performed to study non-isothermal non-adiabatic reactive transport in a low tube-to-particle diameter ratio ($N = 5$) packed bed reactor consisting of 340 spherical particles randomly packed inside, with the objective being to capture the unique phenomena exhibited by gas-solid catalyzed systems experiencing intra-particle diffusion limitations. A grid resolution of 20 cells across the particle radius ($G = 20$) is used for all simulations based on the grid dependency analysis presented in the previous section. In order to portray this, the dimensionless numbers presented in Table (5) were fixed for all 5 simulations conducted. In principle, the parameters γ and β vary spatially throughout the reactor as the temperature has spatial gradients, which in return influences the value of the Thiele modulus ϕ to vary across the reactor. However, the values of γ and β presented in Table (5) is non-dimensionalized using the inlet feed temperature, T_o. The Thiele modulus that is reported, $\phi_o = R_{sp}\sqrt{\frac{k_o}{D_s}}$ is computed using the reaction rate constant at T_o. The settings chosen in Table (5) are based on the McGreavy and Thornton [47] stability analysis who showed that the performance of a reactor may be determined based on a new form of the Thiele modulus non-dimensionalized using the Arrhenius pre-factor A rather than the classical definition. The term $R_{sp}\sqrt{\frac{A}{D_s}}$ has a fixed value across the reactor while the term $R_{sp}\sqrt{\frac{k}{D_s}}$ has spatial gradients dependent on the local temperature value. Thus having fixed the base dimensionless parameters presented in Table (5) to be constant for all 5 simulations, the Arrhenius pre-factor is changed systematically such that $\phi_o = 0.5, 1.0, 2.0, 3.0, 5.0$ for the 5 cases studied respectively.

Another aspect which is taken into consideration is the multiplicity of steady states of individual catalyst particles experiencing interphase

Table 4
Grid dependency study for the Graetz-Nusselt problems.

Case	Grid resolution	Nu (DNS)	Nu (Analytical)	Error
Constant temperature	$G = 10$	3.667	3.657	0.27%
Constant temperature	$G = 40$	3.657	–	~0%
Constant Flux	$G = 10$	4.545	4.364	4.15%
Constant Flux	$G = 40$	4.387	–	0.53%

Table 5
Dimensionless numbers and their values used for the simulation of the full bed reactor.

Dimensionless number	Definition	Value
Reynolds number	$Re = \frac{v_{in}(2R_{sp})}{\nu}$	100
Prandtl number	$Pr = \frac{C_{pf}\mu}{k_f}$	1
Schmidt number	$Sc = \frac{\nu}{D_f}$	1
fluid-to-solid thermal conductivity	$\frac{k_f}{k_s}$	0.1
fluid-to-solid molecular diffusivity	$\frac{D_f}{D_s}$	5
wall-to-inlet temperature ratio	$\frac{T_{cyl}}{T_0}$	1
Arrhenius number	$\gamma = \frac{E}{RT_0}$	20
Prater number	$\beta = \frac{c_0(-\Delta H)D_s}{k_s T_0}$	0.02

and intra-particle gradients. It has been shown by Cresswell [7] that a spherical particle experiencing inter-phase and intra-phase gradients has a unique steady state solution if the following criterion is satisfied

$$\gamma\beta < 8\left(\frac{Bi_h}{Bi_m} + \beta\right) \tag{46}$$

where γ and β chosen here satisfies Cresswell's parametric study range (γ: 10 − 40;β: 0 − 0.1;Bi_h: 0.1 − 10;Bi_m: 100 − 500) where $Bi_h = \frac{h_f R_{sp}}{k_s}$ and $Bi_m = \frac{k_m R_{sp}}{D_s}$ refer to the heat and mass Biot numbers respectively. These parametric values are generally obtained in heterogeneous gas-solid catalyzed systems where k_m and h_f are usually determined empirically. For systems with Lewis number unity ($Le = \frac{Sc}{Pr} = 1$) such as the one considered here, the Sherwood number ($Sh = \frac{k_m 2R_{sp}}{D_f}$) equals the Nusselt number ($Nu = \frac{h_f 2R_{sp}}{k_f}$) [48]. Thus the ratio of the Biot numbers are given by

$$\frac{Bi_h}{Bi_m} = Nu\frac{k_f}{k_s}\frac{1}{Sh}\frac{D_s}{D_f} = \frac{k_f}{k_s}\frac{D_s}{D_f} \tag{47}$$

which would then yield $\frac{Bi_h}{Bi_m} = 0.02$. Thus substituting the parametric values into Eq. (46) gives

$$\gamma\beta = 0.4;8\left(\frac{Bi_h}{Bi_m} + \beta\right) = 0.32 \tag{48}$$

thus dissatisfying Cresswell's criterion with the particles potentially having multiple steady states. A final aspect on stability is the issue of local and global stability [47]. Local stability refers to the ignition and extinction of individual particles while global stability analyzes the system from the macroscopic point of view, where the reactor as a whole may exhibit multiple steady states due to the ignition/extinction of all individual particles. An entire packed bed reactor may exhibit multiple steady states depending on how the reactor is started up; however, the window of operation for such a behavior is extremely narrow and impractical in large-scale reactors [49]. Thus the issue of global stability is not addressed in this work.

Each individual particle in the packed bed reactor under steady state conditions should satisfy the heat balance given by the following expression

$$h_f(T_{avg} - \langle T_f \rangle) = k_m(c_{avg} - \langle c_f \rangle)(\Delta H) \tag{49}$$

where T_{avg} and c_{avg} refer to the average surface temperature and concentration values of the particle respectively. $\langle T_f \rangle$ and $\langle c_f \rangle$ refer to the corresponding bulk fluid temperature and concentration values surrounding the thin film resisting the transport of heat and mass towards the surface of the particle. It was reported earlier that under the conditions of no external transport limitations ($Bi_m \to \infty$, $Bi_h \to \infty$), the maximal temperature rise within a catalyst pellet is governed by $\frac{T_{max} - T_{avg}}{T_{avg}} = \beta = \frac{c_0(-\Delta H)D_s}{k_s T_0}$ where the underlying assumption is that $T_{avg} = T_o$ and $c_{avg} = c_o$ with T_o and c_o being the inlet feed temperature and concentration respectively. While the mass Biot number is generally very large, this is generally not the case for the heat Biot numbers in gas-solid systems. It was shown by Carberry [48] that when a system does experience interphase gradients, the maximal temperature rise in a catalyst can exceed β when $\frac{Bi_m}{Bi_h} \gg 1$ which is generally the case for gas-solid systems. This happens when the thin film of heat transfer resistance cooling the catalyst particle breaks during ignition leading to a rapid temperature rise within the catalyst. Hatfield and Aris [50] set forth *a priori* bounds on the maximal temperature rise within a catalyst experiencing interphase gradients with $\frac{Bi_m}{Bi_h} \gg 1$ as follows

$$1 \leqslant \frac{T_{avg}}{T_o} \leqslant 1 + \beta \mathrm{Max}\left\{1, \frac{Bi_m}{Bi_h}\right\} \tag{50}$$

Thus the maximum dimensionless temperature possible within the reactor at steady state for the current system $\left(\frac{Bi_m}{Bi_h} = 50\right)$ would be

$$\frac{T_{max}}{T_o} = 1 + \beta\frac{Bi_m}{Bi_h} = 2 \tag{51}$$

Furthermore, another important observation from the Hatfield and Aris [50] analysis is the significance of the ratio $\frac{Bi_m}{Bi_h}$. The greater the value of $\frac{Bi_m}{Bi_h}$, the greater is the maximal dimensionless temperature rise across the catalyst. Such large ratios are generally observed when a system experiences large intra-particle mass transfer resistances (ex - Fischer-Tropsch synthesis), with pore diffusion actually enhancing the exothermic nature of the system resulting in larger temperature gradients.

4.1. Ignition and extinction phenomena

The steady state contour plots of velocity, dimensionless temperature ($T^* = \frac{T}{T_0}$) and dimensionless concentration ($c^* = \frac{c}{c_0}$) for the $\phi_o = 0.5$ case is presented in Fig. 7. A negligible temperature and concentration gradient is observed across the length of the reactor with $\frac{T_{max}}{T_0} \approx 1 + \beta$ [50]. The system has a unique steady state solution (globally stable) and the rate of reaction is not fast enough for the particles to self-ignite. Thus the reactor is said to be in a state of extinction. The flow-averaged dimensionless concentration and temperature along the axial direction is plotted in Fig. 8 where

$$c_b^*(x) = \frac{\iint_{S_f} c^* v_x dS}{\iint_{S_f} v_x dS}; \quad T_b^*(x) = \frac{\iint_{S_f} T^* v_x dS}{\iint_{S_f} v_x dS} \tag{52}$$

with S_f referring to the cross-sectional area occupied by the fluid along the x coordinate, being the direction of macroscopic flow. The dimensionless axial superficial velocity distribution ($v_x^*(r)$) across the cross-sectional radius of the reactor is presented in Fig. 8 whose value is averaged across the length of the reactor with

$$v_x^*(r) = \frac{1}{v_{in}}\frac{\iint v_x(r) dx d\theta}{\iint dx d\theta} \tag{53}$$

The effect of flow-maldistribution is clearly visible due to the porosity distribution across the radius with the channeling of flow along the reactor wall being prominent with v_{in} being the inlet velocity. The radial concentration and temperature contour plots at 3 different axial positions are presented in Fig. 9 and the corresponding profiles are depicted in Fig. 10. In Fig. 10 it is observed that the radial gradients of concentration and temperature are not monotonic in nature. This non-monotonic behaviour can be related to various factors with the most important one being the local packing structure of the particles within the bed. Local sharp gradients in temperature and concentration also contributes to the non-monotonic behaviour. Now, we may define a

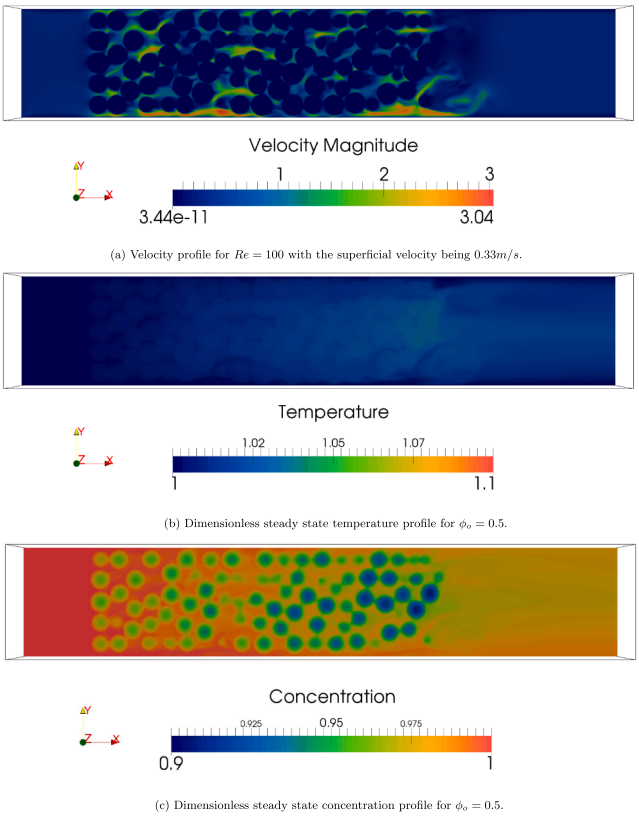

(a) Velocity profile for $Re = 100$ with the superficial velocity being $0.33 m/s$.

(b) Dimensionless steady state temperature profile for $\phi_o = 0.5$.

(c) Dimensionless steady state concentration profile for $\phi_o = 0.5$.

Fig. 7. Steady state contour plots of velocity, heat and mass of the packed bed reactor for the $\phi_o = 0.5$ case.

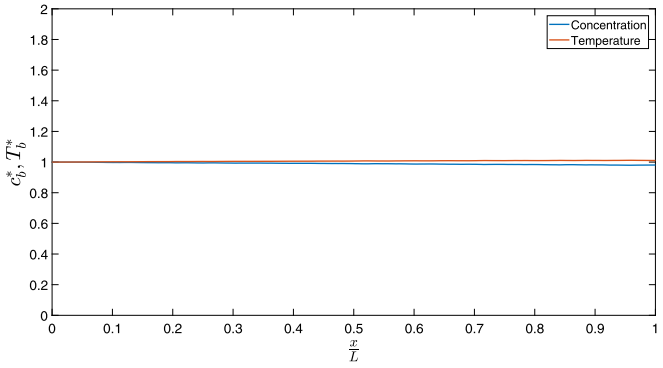

(a) Axial bulk temperature and concentration profiles.

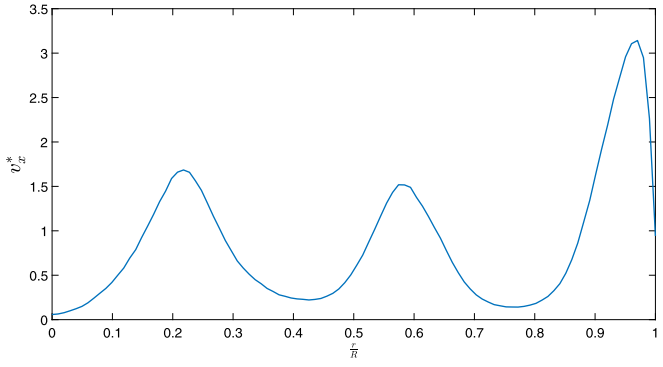

(b) Radial distribution of axial superficial velocity.

Fig. 8. Steady state dimensionless profiles for the $\phi_o = 0.5$ case.

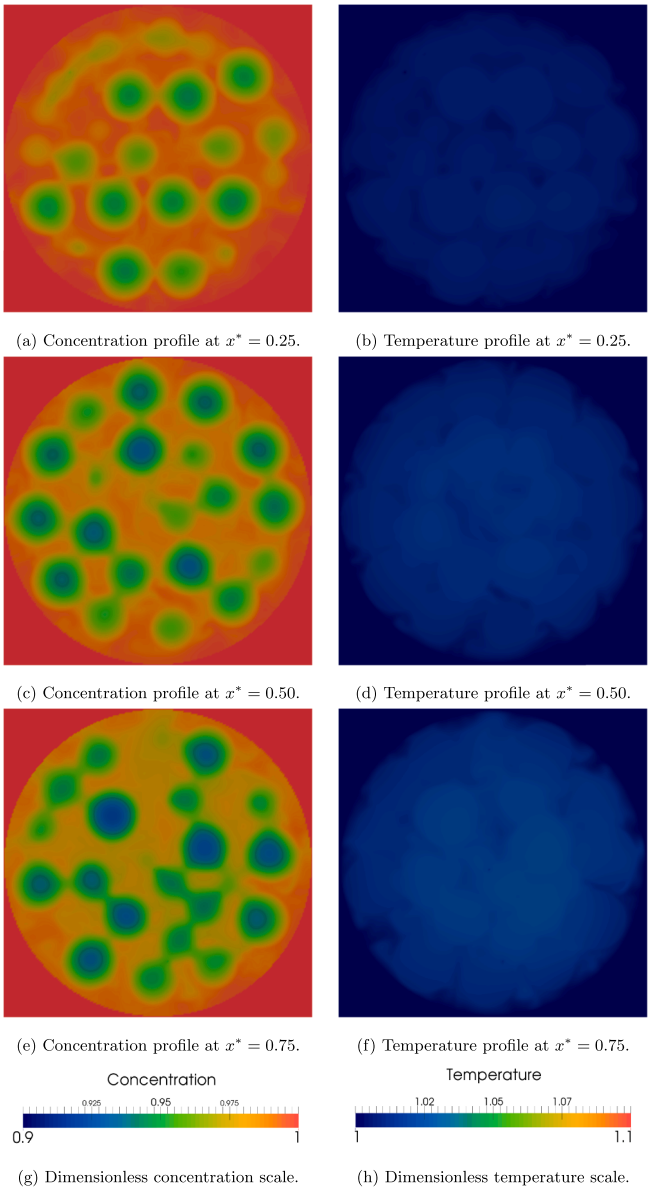

(a) Concentration profile at $x^* = 0.25$.

(b) Temperature profile at $x^* = 0.25$.

(c) Concentration profile at $x^* = 0.50$.

(d) Temperature profile at $x^* = 0.50$.

(e) Concentration profile at $x^* = 0.75$.

(f) Temperature profile at $x^* = 0.75$.

(g) Dimensionless concentration scale.

(h) Dimensionless temperature scale.

Fig. 9. Radial contour plots at different axial positions for $\phi_o = 0.5$ case.

total effectiveness factor to evaluate the enhancement in the reaction rate due to the exothermic nature of the system as follows:

$$\bar{\eta} = \frac{\iint \int_{V_s} r_s dV}{V_s k_o c_o} \tag{54}$$

where V_s refers to the volume of solid catalysts present within the reactor. $\bar{\eta}$ was to found to be equal to 1.25 for the $\phi_o = 0.5$ case suggesting a slight enhancement in the reaction rate as compared to the reaction being carried out at inlet conditions.

Upon increasing the rate of reaction to $\phi_o = 1$ and keeping all other parameters same as before, we observe the appearance of creeping reaction zones [9]. The particles at the end of the reactor first start to self-ignite followed by a high temperature wave that moves in the upstream direction igniting the particles in the core of the bed. The contour plots depicting the moving reaction zone are presented in Figs. 11 and 12. The reaction front almost propagates towards the entrance of the reactor and eventually reaches steady state with intermediate conversion as seen in Fig. 13a where the temporal evolution of the dimensionless bulk temperature is plotted. Some of the particles reside in the lower steady state while the rest of the particles are in the higher steady state

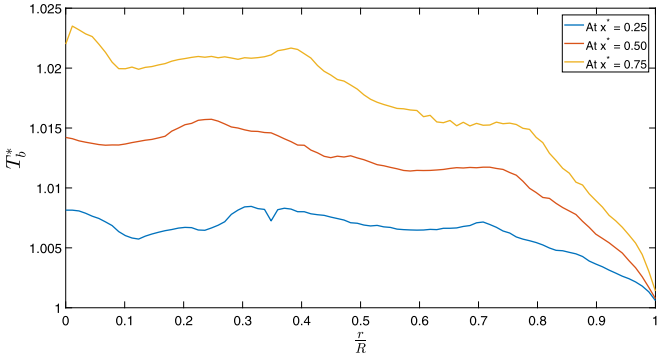

(a) Dimenionless temperature profile.

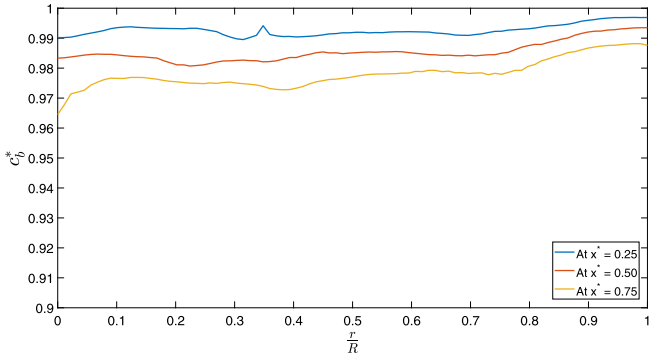

(b) Dimensionless concentration profile.

Fig. 10. Radial profiles at different axial positions for $\phi_o = 0.5$ case.

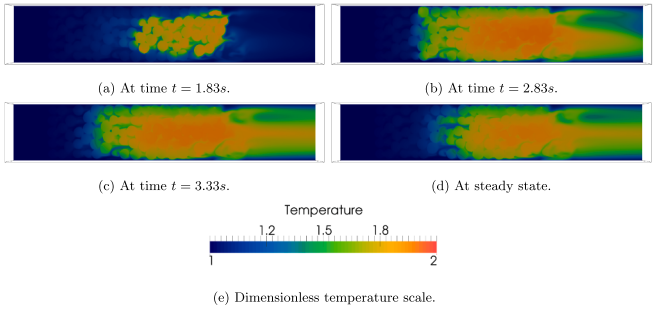

(a) At time $t = 1.83s$. (b) At time $t = 2.83s$. (c) At time $t = 3.33s$. (d) At steady state. (e) Dimensionless temperature scale.

Fig. 11. Contour plots depicting the temporal evolution of the dimensionless temperature profile for the $\phi_o = 1.0$.

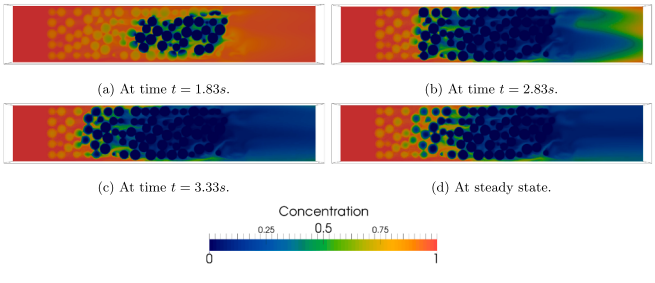

(a) At time $t = 1.83s$. (b) At time $t = 2.83s$. (c) At time $t = 3.33s$. (d) At steady state. (e) Dimensionless concentration scale.

Fig. 12. Contour plots depicting the temporal evolution of the dimensionless concentration profile for the $\phi_o = 1.0$.

(≈ 65%). The corresponding dimensionless radial concentration profiles are presented in Fig. 13b which are in accordance with the temperature evolution. The moving reaction zone phenomena has been studied extensively previously primarily using 1-D models [51–53] with Partopour and Dixon [38] recently studying the wrong-way behavior of packed beds using a DNS model. The DNS model inherently accounts

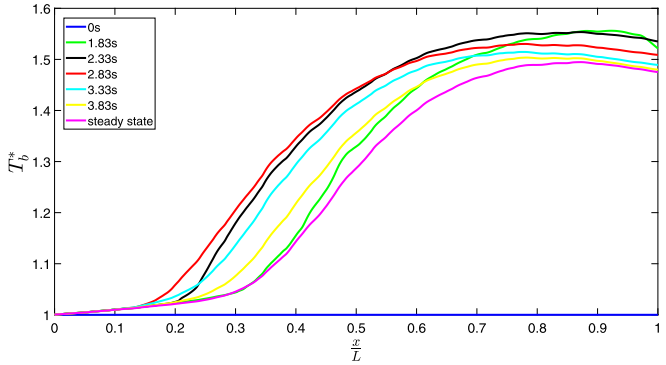

(a) Evolution of the temperature profile.

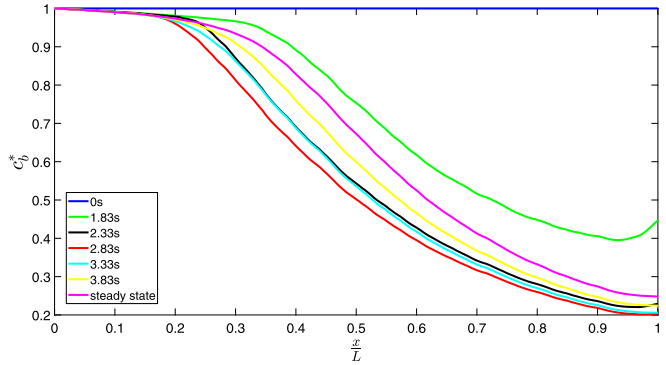

(b) Evolution of the concentration profile.

Fig. 13. Creeping reaction zones observed for the $\phi_o = 1.0$ case.

for axial thermal dispersion which is the main driving mechanism for the moving reaction zone [54] while the classical models require the incorporation of the axial heat dispersion coefficient to accurately capture this phenomena. The catalyst particles in the DNS model form a single continuous phase that accounts for particle-particle heat conduction, thus driving the reaction front against the direction of flow. The radial contour plots along 3 different axial cross-sections are presented in Fig. 14 and their corresponding profiles are plotted in Fig. 15. The calculated total effectiveness factor, $\bar{\eta}$, was found to be equal to 14.13 implying a significant enhancement in the reaction rate due to most of the particles residing at the higher steady-state.

As the reaction rate is increased to $\phi_o > 1$ we observe that all the particles in the reactor get ignited followed by the formation of a *hot-spot* at steady state. Furthermore, we observe that the dimensionless profiles for cases $\phi_o = 2, 3, 5$ are almost identical with the curves superimposing as observed in Fig. 16. The reactor is now fully controlled by external transport limitations with the main resistance provided by the thin fluid film surrounding the particles inhibiting the transport of reactants to the catalyst. The total effectiveness factor $\bar{\eta}$ for the 3 cases was found to be 7.05, 3.91, 1.81 respectively with the effectiveness factor decreasing upon increasing the reaction rate with the exothermicity playing a less prominent role at high Thiele Moduli. The contour plots of the reactor is presented in Fig. 17. For the $\phi_o > 1$ cases, the rate of reaction is so large that all the particles get ignited simultaneously across the length of the reactor followed by a large temperature rise in the fluid phase. The $T_b^*(x)$ curve then exhibits a maximum followed by the cooling of the particles at the downstream section of the reactor. The temporal evolution of the concentrations and temperature profiles are depicted in Fig. 18a and b respectively.

4.2. Comparison with a 1-D heterogeneous model

In this subsection, the results from the Direct Numerical Simulation model are compared with a simple 1-D heterogeneous reactor model employing empirical correlations to qualitatively and quantitatively

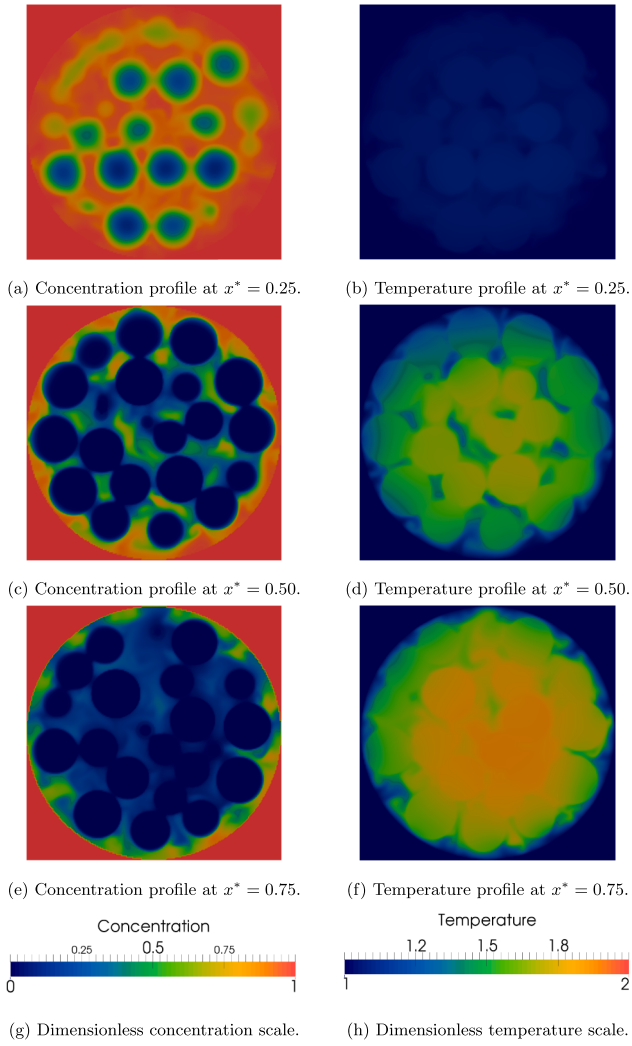

(a) Concentration profile at $x^* = 0.25$. (b) Temperature profile at $x^* = 0.25$.

(c) Concentration profile at $x^* = 0.50$. (d) Temperature profile at $x^* = 0.50$.

(e) Concentration profile at $x^* = 0.75$. (f) Temperature profile at $x^* = 0.75$.

(g) Dimensionless concentration scale. (h) Dimensionless temperature scale.

Fig. 14. Radial contour plots at different axial positions for $\phi_o = 1.0$ case.

assess the performance of DNS against well-established models. The 1-D model assumes plug-flow in the fluid phase where the fluid phase concentration and temperature is coupled to a particle model via the interphase heat and mass transfer coefficients. The description of the heterogeneous reactor model is provided in the Appendix and is closed by 3 empirical correlations being the Sherwood/Nusselt numbers by Gunn [55], the heat and mass dispersion coefficients by Edwards and Richardson [56] and the wall-to-bed heat transfer coefficient by Yagi and Wakao [57]. All parameters presented in Table (4) for the DNS model are consistent with the inputs for the 1-D model. The three cases considered are $\phi_o = 0.5$, 1.0, 3.0 as they represent the 3 distinct regimes simulated. The results of the comparison are presented in Fig. 19. It is observed that the DNS model qualitatively replicates the empirical 1-D model with exceptional accuracy by predicting the ignition and extinction phenomena and the creeping reaction zone for the $\phi_o = 1.0$ case. The DNS model quantitatively predicts the 1-D model very accurately for the $\phi_o = 0.5$ as the temperature gradients within the reactor are small and thus resulting in very low conversion. For the $\phi_o = 1.0$ case, the 1-D model overpredicts the temperature rise and the conversion across the reactor as compared to the DNS model. This arises primarily from the temperature gradients across the reactor as higher temperatures leads to higher conversion and vice-versa. Furthermore, another major assumption which affects the quantitative differences between the two models is the consideration of plug-flow in the 1-D model whereby the channeling effect which provides an extra resistance in the heat removal process is neglected. The quantitative

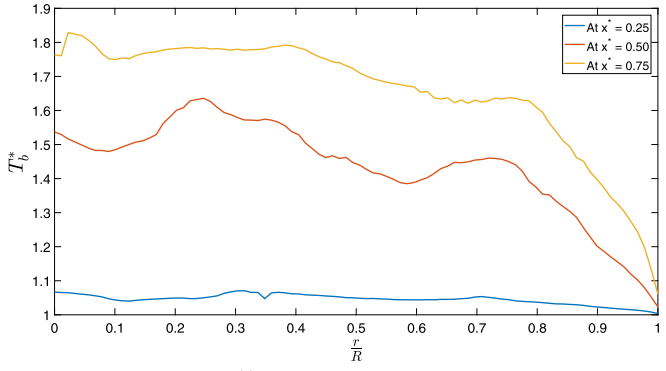

(a) Dimenionless temperature profile.

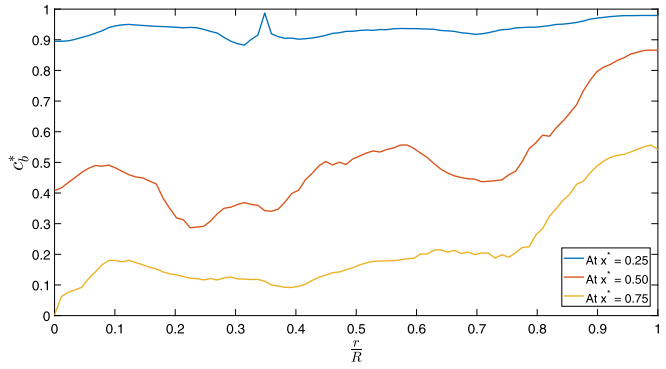

(b) Dimensionless concentration profile.

Fig. 15. Radial profiles at different axial positions for $\phi_o = 1.0$ case.

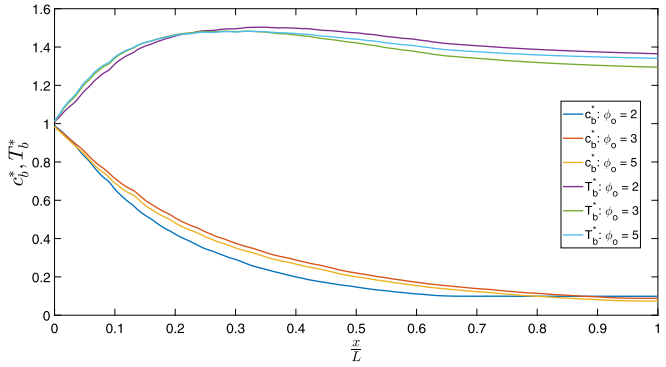

Fig. 16. Steady state dimensionless profiles for $\phi_o = 3.0$.

deviations increase for the $\phi_o = 3.0$ case and the reasons may be attributed to the above mentioned reasons. Of the 3 empirical parameters used in the 1-D model, the axial mass dispersion coefficient plays an almost negligible role in the performance of the model while the axial dispersion coefficient does play a significant role in controlling the hot-spot magnitude. This essentially is due to the finite size of the bed length considered. The heat and mass transfer coefficients play a slightly less prominent role in the performance of the reactor as when compared to the wall-to-bed heat transfer coefficient. The wall-to-bed heat transfer dictates the temperature gradients within the reactor and thus in return control the conversion across the bed. The wall-to-bed Nusselt number (Nu_w) is evaluated from the DNS model and compared with the Yagi and Wakao [57] correlation. The wall-to-bed heat transfer coefficient across the cylinder cross-section along the direction of macroscopic flow (x) is evaluated as follows

$$h_w = \frac{-k_f \frac{\partial T_f}{\partial r}_{r=R_{cyl}}}{T_{cyl} - T_b} \tag{55}$$

The wall-to-bed Nusselt number is calculated as

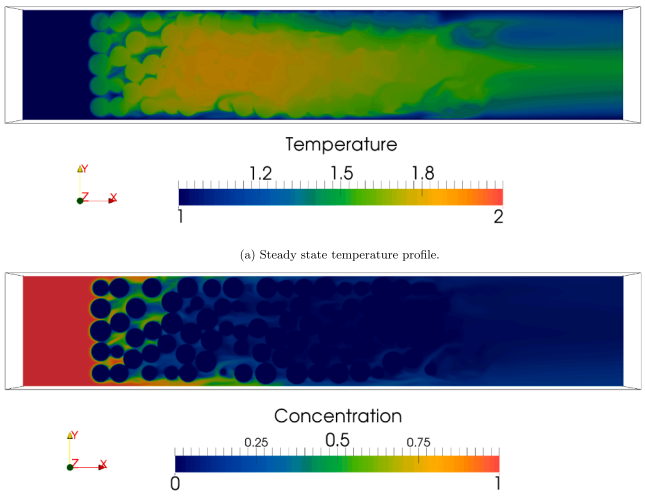

(a) Steady state temperature profile.

(b) Steady state concentration profile.

Fig. 17. Steady state contour plots of concentration and temperature for the $\phi_o = 3.0$ case.

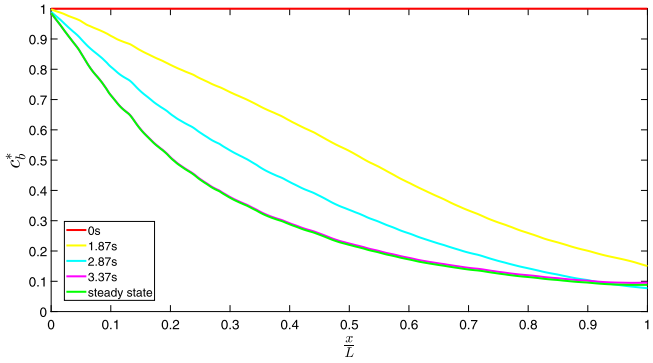

(a) Evolution of the concentration profile.

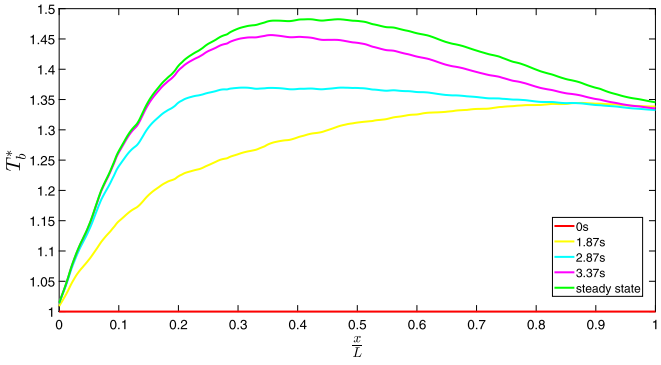

(b) Formation of the hot-spot.

Fig. 18. Temporal evolution of the reactor for the $\phi_o = 3.0$ case.

$$Nu_w = \frac{h_w(2R_{sp})}{k_f} \tag{56}$$

The Nusselt numbers evaluated from the DNS results for the 3 different cases are plotted in Fig. 20 and the calculated values are in good agreement with the empirical correlation. Furthermore, it is observed that the rate of reaction has a negligible effect on the heat removal process from the wall.

5. Conclusion

A novel numerical model that is free of empiricism was developed to simulate a non-isothermal catalytic reactor. The model accounts for the coupled interaction between the solid phase and the fluid phase by imposing the appropriate interface boundary conditions using an Immersed Boundary Method. The model was validated with existing well-established cases for single-particle systems to ensure the accurate incorporation of intra-particle heat and mass transport and its coupling to the fluid phase. A non-adiabatic reactor consisting of 340 particles was simulated where the random packing was generated using the Discrete Element Method.

A key feature of the numerical procedure presented in this work is the intrinsic coupling between the fluid phase transport and the solid

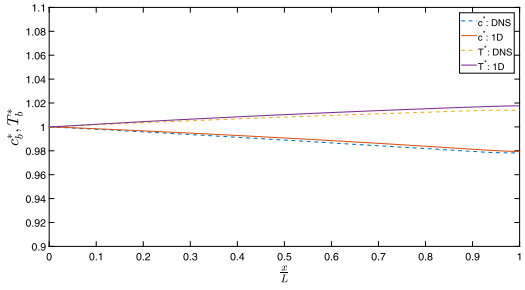

(a) Dimensionless steady state concentration and temperature profiles for the $\phi_o = 0.5$ case.

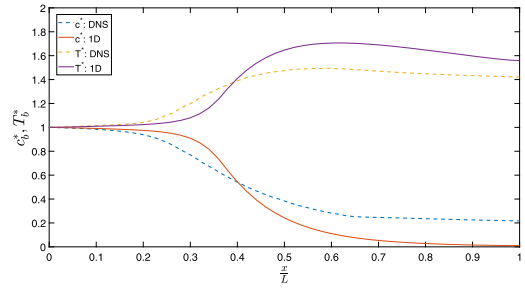

(b) Dimensionless steady state concentration and temperature profiles for the $\phi_o = 1.0$ case.

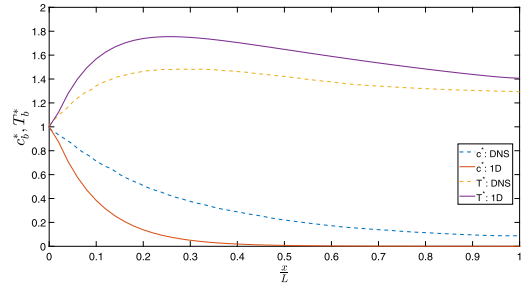

(c) Dimensionless steady state concentration and temperature profiles for the $\phi_o = 3.0$ case.

Fig. 19. Comparison of the dimensionless bulk temperature and concentration profiles obtained from DNS against the results from a 1-D heterogeneous model.

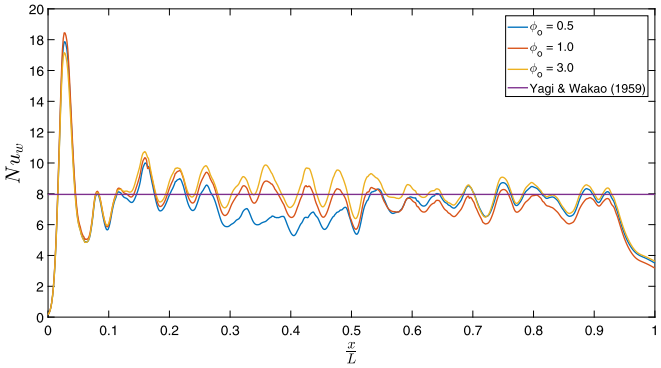

Fig. 20. Wall-to-bed Nusselt numbers evaluated using the DNS results for 3 different cases compared against the empirical correlation by Yagi and Wakao [57].

phase transport incorporated using the Immersed Boundary technique. During exothermic catalytic reactions, the heat produced within the catalyst phase causes a large transient temperature rise in the fluid phase accounted for via the continuity of heat fluxes between the two phases. Under non-adiabatic conditions, a hot-spot is formed within the reactor whose magnitude is dictated only by the kinetic and transport parameter values. Unlike the classical phenomenological models where the inputted empirical parameters such as wall-to-bed heat transfer coefficient, h_w, and radial thermal dispersion coefficient, k_r, control the hot-spot magnitude, the DNS model inherently accounts for these features thus avoiding the uncertainties involved in the accuracies of these empirical coefficients. It was also observed and shown that the effectiveness factor within the catalytic system can exceed unity due to the autothermal reaction being carried out and that the assumption that intra-particle mass transport can be modelled using the simple expression given by Eq. (32) may not be valid when performing DNS of exothermic systems.

Finally, the simulations conducted in this work on the full bed reactor reveal the model's capability to simulate the transient dynamics of an exothermic catalytic system. Furthermore, a stability analysis is performed to capture the phenomena of ignition and extinction of a wall cooled reactor where the particles may be locally unstable due to the existence of multiple steady states. The current developed model signifies the importance of accounting for intra-particle gradients of coupled heat and mass while studying exothermic catalytic reactions, whereby, its negligence may yield qualitatively different results. The exothermicity of the system can have many other implications on the performance of the reactor with one good example being deviations from ideality. A strong consequence of high temperature gradients would result in changes of the viscosity of the fluid having an exponential dependency and large temperature changes may also induce compressibility effects which cannot then be neglected within the model and these considerations shall be addressed in future works.

Declaration of Competing Interest

The authors declare that they have no known competing financial interests or personal relationships that could have appeared to influence the work reported in this paper.

Acknowledgement

This work was supported by the Netherlands Center for Multiscale Catalytic Energy Conversion (MCEC), an NWO Gravitation programme funded by the Ministry of Education, Culture and Science of the government of the Netherlands. This work was carried out on the Dutch national e-infrastructure with the support of SURF Cooperative. The authors thank SURF SARA (www.surfsara.nl) and NWO for the support in using the Cartesius supercomputer.

Appendix A

The 1-D heterogeneous plug-flow model used for comparison with the DNS results assuming steady state for the fluid phase concentration reads

$$v_x \frac{\partial \bar{C}_f}{\partial x} = D_{ax} \frac{\partial^2 \bar{C}_f}{\partial x^2} + (1-\varepsilon)\frac{3}{R_{sp}} k_m (\bar{C}_s - \bar{C}_f) \tag{57}$$

The fluid phase temperature reads

$$\rho_f C_{pf} v_x \frac{\partial \bar{T}_f}{\partial x} = k_{ax} \frac{\partial^2 \bar{T}_f}{\partial x^2} - h_w \frac{2}{R_{cyl}} (\bar{T}_f - T_{cyl}) + (1-\varepsilon)\frac{3}{R_{sp}} h_f (\bar{T}_s - \bar{T}_f) \tag{58}$$

The particle phase concentration reads

$$0 = D_s \frac{1}{r^2}\left[\frac{\partial}{\partial r}\left(r^2 \frac{\partial \bar{C}_s}{\partial r}\right)\right] - k\bar{C}_s \tag{59}$$

The particle phase temperature reads

$$0 = k_s \frac{1}{r^2}\left[\frac{\partial}{\partial r}\left(r^2 \frac{\partial \bar{T}_s}{\partial r}\right)\right] - k\bar{C}_s(\Delta H) \tag{60}$$

The boundary conditions used for closing the above system of governing equations are

$$\bar{C}_f(x=0) = c_o; \quad \frac{\partial \bar{C}_f}{\partial x}(x=L) = 0 \tag{61}$$

$$\bar{T}_f(x=0) = T_o; \quad \frac{\partial \bar{T}_f}{\partial x}(x=L) = 0 \tag{62}$$

$$-D_s \frac{\partial \bar{C}_s}{\partial r}(r=o) = 0; \quad -D_s \frac{\partial \bar{C}_s}{\partial r}(r=R_{sp}) = k_m(\bar{C}_s - \bar{C}_f) \tag{63}$$

$$-k_s \frac{\partial \bar{T}_s}{\partial r}(r=o) = 0; \quad -k_s \frac{\partial \bar{T}_s}{\partial r}(r=R_{sp}) = h_f(\bar{T}_s - \bar{T}_f) \tag{64}$$

3 empirical correlations are used for estimating D_{ax}, k_{ax}, h_f, k_m, h_w to complete the above described 1-D model.

The Edwards and Richardson [56] correlation to estimate the axial dispersion coefficients

$$D_{ax} = 0.73 D_f + \frac{0.5 v_{in} d_{sp}}{1 + \frac{9.7 D_f}{v_{in} d_{sp}}} \tag{65}$$

and assuming $\frac{D_{ax}}{D_f} = \frac{k_{ax}}{k_f}$.

The Edwards and Richardson [55] correlation to estimate the fluid to particle heat and mass transfer coefficients

$$Nu = (7 - 10\varepsilon + 5\varepsilon^2)(1 + 0.7Re^{0.2}\,Pr^{0.33}) + (1.33 - 2.4\varepsilon + 1.2\varepsilon^2)Re^{0.7}\,Pr^{0.33} \quad (66)$$

with $Nu = Sh$ for cases when $Pr = Sc$ wherein we have $Nu = \frac{h_f(2R_{sp})}{k_f}$ and $Sh = \frac{k_m(2R_{sp})}{D_f}$.

The correlation by Yagi and Wakao [57] is used for estimating the wall-to-bed heat transfer with the wall Nusselt number (Nu_w) given by

$$Nu_w = 0.6Re^{0.5}(Re < 40); \quad Nu_w = 0.2Re^{0.8}(Re > 40) \quad (67)$$

where $Nu_w = \frac{h_w(2R_{sp})}{k_f}$.

References

[1] O. Galan, V.G. Gomes, J. Romagnoli, K.F. Ngian, Selective oxidation of ethylene in an industrial packed-bed reactor: modelling, analysis and optimization, Int. J. Chem. Reactor Eng. 7(1).
[2] J. Hoebink, P. Couwenberg, G. Marin, Fixed bed reactor design for gas phase chain reactions catalysed by solids: the oxidative coupling of methane, Chem. Eng. Sci. 49 (24) (1994) 5453–5463.
[3] J. Papageorgiou, G. Froment, Phthalic anhydride synthesis. Reactor optimization aspects, Chem. Eng. Sci. 51 (10) (1996) 2091–2098.
[4] O. Bilous, N.R. Amundson, Chemical reactor stability and sensitivity, AIChE J. 1 (4) (1955) 513–521.
[5] C. Van Heerden, The character of the stationary state of exothermic processes, Chem. Eng. Sci. 8 (1–2) (1958) 133–145.
[6] P. Weisz, J. Hicks, The behaviour of porous catalyst particles in view of internal mass and heat diffusion effects, Chem. Eng. Sci. 17 (4) (1962) 265–275.
[7] D.L. Cresswell, On the uniqueness of the steady state of a catalyst pellet involving both intraphase and interphase transport, Chem. Eng. Sci. 25 (2) (1970) 267–275.
[8] S.-L. Liu, N.R. Amundson, Stability of adiabatic packed bed reactors. An elementary treatment, Ind. Eng. Chem. Fundam. 1 (3) (1962) 200–208.
[9] G. Eigenberger, On the dynamic behavior of the catalytic fixed-bed reactor in the region of multiple steady states-I. The influence of heat conduction in two phase models, Chem. Eng. Sci. 27 (11) (1972) 1909–1915.
[10] J.J. Carberry, D. White, On the role of transport phenomena in catalytic reactor behavior, Ind. Eng. Chem. 61 (7) (1969) 27–35.
[11] A.P. De Wasch, G.F. Froment, A two dimensional heterogeneous model for fixed bed catalytic reactors, Chem. Eng. Sci. 26 (5) (1971) 629–634.
[12] C. McGreavy, D.L. Cresswell, A lumped parameter approximation to a general model for catalytic reactors, Can. J. Chem. Eng. 47 (6) (1969) 583–589.
[13] G.F. Froment, Fixed bed catalytic reactors-current design status, Ind. Eng. Chem. 59 (2) (1967) 18–27.
[14] W. Paterson, J.J. Carberry, Fixed bed catalytic reactor modelling: the heat transfer problem, Chem. Eng. Sci. 38 (1) (1983) 175–180.
[15] J.J. Lerou, G.F. Froment, Velocity, temperature and conversion profiles in fixed bed catalytic reactors, Chem. Eng. Sci. 32 (8) (1977) 853–861.
[16] R.F. Benenati, C.B. Brosilow, Void fraction distribution in beds of spheres, AIChE J. 8 (3) (1962) 359–361.
[17] P. Zehner, E.U. Schlunder, Thermal conductivity of packings at moderate temperatures, Chem. Ing. Tech. 42 (14) (1970) 933–+.
[18] O. Kalthoff, D. Vortmeyer, Ignition/extinction phenomena in a wall cooled fixed bed reactor: experiments and model calculations including radial porosity and velocity distributions, Chem. Eng. Sci. 35 (7) (1980) 1637–1643.
[19] D. Vortmeyer, J. Schuster, Evaluation of steady flow profiles in rectangular and circular packed beds by a variational method, Chem. Eng. Sci. 38 (10) (1983) 1691–1699.
[20] P. Cheng, D. Vortmeyer, Transverse thermal dispersion and wall channelling in a packed bed with forced convective flow, Chem. Eng. Sci. 43 (9) (1988) 2523–2532.
[21] D. Vortmeyer, E. Haidegger, Discrimination of three approaches to evaluate heat fluxes for wall-cooled fixed bed chemical reactors, Chem. Eng. Sci. 46 (10) (1991) 2651–2660.
[22] A.G. Dixon, Fixed bed catalytic reactor modelling-the radial heat transfer problem, Can. J. Chem. Eng. 90 (3) (2012) 507–527.
[23] M. Winterberg, E. Tsotsas, A. Krischke, D. Vortmeyer, A simple and coherent set of coefficients for modelling of heat and mass transport with and without chemical reaction in tubes filled with spheres, Chem. Eng. Sci. 55 (5) (2000) 967–979.
[24] M.P. Dudukovic, Frontiers in reactor engineering, Science 325 (5941) (2009) 698–701.
[25] N.G. Deen, E.A.J.F. Peters, J.T. Padding, J.A.M. Kuipers, Review of Direct Numerical Simulation of fluid–particle mass, momentum and heat transfer in dense gas–solid flows, Chem. Eng. Sci. 116 (2014) 710–724.
[26] B. Sun, S. Tenneti, S. Subramaniam, D.L. Koch, Pseudo-turbulent heat flux and average gas–phase conduction during gas–solid heat transfer: flow past random fixed particle assemblies, J. Fluid Mech. 798 (2016) 299–349.
[27] Y. Tang, E.A.J.F. Peters, J.A.M. Kuipers, S.H.L. Kriebitzsch, M.A. van der Hoef, A new drag correlation from fully resolved simulations of flow past monodisperse static arrays of spheres, AIChE J. 61 (2) (2015) 688–698.
[28] H. Tavassoli, S. Kriebitzsch, M. Van der Hoef, E.A.J.F. Peters, J.A.M. Kuipers, Direct numerical simulation of particulate flow with heat transfer, Int. J. Multiph. Flow 57 (2013) 29–37.
[29] S. Das, N.G. Deen, J.A.M. Kuipers, A DNS study of flow and heat transfer through slender fixed-bed reactors randomly packed with spherical particles, Chem. Eng. Sci. 160 (2017) 1–19.
[30] V. Chandra, S. Das, E.A.J.F. Peters, J.A.M. Kuipers, Direct numerical simulation of hydrodynamic dispersion in open-cell solid foams, Chem. Eng. J. 358 (2019) 1305–1323.
[31] A.G. Dixon, M. Nijemeisland, E.H. Stitt, Packed tubular reactor modeling and catalyst design using computational fluid dynamics, Adv. Chem. Eng. 31 (2006) 307–389.
[32] N. Jurtz, M. Kraume, G.D. Wehinger, Advances in fixed-bed reactor modeling using particle-resolved computational fluid dynamics (CFD), Rev. Chem. Eng. 35 (2) (2019) 139–190.
[33] A.G. Dixon, Local transport and reaction rates in a fixed bed reactor tube: Endothermic steam methane reforming, Chem. Eng. Sci. 168 (2017) 156–177.
[34] A.G. Dixon, M.E. Taskin, E.H. Stitt, M. Nijemeisland, 3D CFD simulations of steam reforming with resolved intraparticle reaction and gradients, Chem. Eng. Sci. 62 (18–20) (2007) 4963–4966.
[35] G.D. Wehinger, F. Klippel, M. Kraume, Modeling pore processes for particle-resolved CFD simulations of catalytic fixed-bed reactors, Comput. Chem. Eng. 101 (2017) 11–22.
[36] T. Maffei, G. Gentile, S. Rebughini, M. Bracconi, F. Manelli, S. Lipp, A. Cuoci, M. Maestri, A multiregion operator-splitting CFD approach for coupling microkinetic modeling with internal porous transport in heterogeneous catalytic reactors, Chem. Eng. J. 283 (2016) 1392–1404.
[37] G.D. Wehinger, T. Eppinger, M. Kraume, Detailed numerical simulations of catalytic fixed-bed reactors: heterogeneous dry reforming of methane, Chem. Eng. Sci. 122 (2015) 197–209.
[38] B. Partopour, A.G. Dixon, Integrated multiscale modeling of fixed bed reactors: studying the reactor under dynamic reaction conditions, Chem. Eng. J.
[39] J. Lu, S. Das, E. Peters, J. Kuipers, Direct numerical simulation of fluid flow and mass transfer in dense fluid-particle systems with surface reactions, Chem. Eng. Sci. 176 (2018) 1–18.
[40] J. Lu, E. Peters, J. Kuipers, Direct numerical simulation of fluid flow and dependently coupled heat and mass transfer in fluid-particle systems, Chem. Eng. Sci. 204 (2019) 203–219.
[41] N.G. Deen, S.H.L. Kriebitzsch, M.A. van der Hoef, J.A.M. Kuipers, Direct Numerical Simulation of flow and heat transfer in dense fluid–particle systems, Chem. Eng. Sci. 81 (2012) 329–344.
[42] S. Das, N.G. Deen, J.A.M. Kuipers, Direct Numerical Simulation for flow and heat transfer through random open-cell solid foams: development of an IBM based CFD model, Catal. Today 273 (2016) 140–150.
[43] N.G. Deen, J.A.M. Kuipers, Direct Numerical Simulation of fluid flow and mass transfer in dense fluid–particle systems, Ind. Eng. Chem. Res. 52 (33) (2013) 11266–11274.
[44] E.W. Thiele, Relation between catalytic activity and size of particle, Ind. Eng. Chem. 31 (7) (1939) 916–920.
[45] M. Sulaiman, A. Hammouti, E. Climent, A. Wachs, Coupling the fictitious domain and sharp interface methods for the simulation of convective mass transfer around reactive particles: towards a reactive Sherwood number correlation for dilute systems, Chem. Eng. Sci. 198 (2019) 334–351.
[46] R.K. Shah, A.L. London, Laminar Flow Forced Convection in Ducts: A Source Book for Compact Heat Exchanger Analytical Data, Academic Press, 2014.
[47] C. McGreavy, J.M. Thornton, Generalised criteria for the stability of catalytic reactors, Can. J. Chem. Eng. 48 (2) (1970) 187–191.
[48] J. Carberry, Yield in chemical reactor engineering, Ind. Eng. Chem. 58 (10) (1966) 40–53.
[49] G.F. Froment, H.P.K. Hofmann, Design of fixed-bed gas-solid catalytic reactors, Chemical Reaction and Reactor Engineering, vol. 373, Marcel Dekker, New York, 1987.
[50] B. Hatfield, R. Aris, Communications on the theory of diffusion and reaction-IV Combined effects of internal and external diffusion in the non-isothermal case, Chem. Eng. Sci. 24 (8) (1969) 1213–1222.
[51] G. Eigenberger, On the dynamic behavior of the catalytic fixed-bed reactor in the region of multiple steady states-II. The influence of the boundary conditions in the catalyst phase, Chem. Eng. Sci. 27 (11) (1972) 1917–1924.
[52] D. Vortmeyer, W. Jahnel, Moving reaction zones in fixed bed reactors under the influence of various parameters, Chem. Eng. Sci. 27 (8) (1972) 1485–1496.
[53] H.-K. Rhee, D. Foley, N.R. Amundson, Creeping reaction zone in a catalytic, fixed-bed reactor: a cell model approach, Chem. Eng. Sci. 28 (2) (1973) 607–615.
[54] V. Pinjala, Y. Chen, D. Luss, Wrong-way behavior of packed-bed reactors: II. Impact of thermal dispersion, AIChE J. 34 (10) (1988) 1663–1672.
[55] D. Gunn, Transfer of heat or mass to particles in fixed and fluidised beds, Int. J. Heat Mass Transf. 21 (4) (1978) 467–476.
[56] M. Edwards, J. Richardson, Gas dispersion in packed beds, Chem. Eng. Sci. 23 (2) (1968) 109–123.
[57] S. Yagi, N. Wakao, Heat and mass transfer from wall to fluid in packed beds, AIChE J. 5 (1) (1959) 79–85.